TITLE

The mitochondrial calcium uniporter is necessary for synaptic plasticity and proper mitochondrial morphology and distribution in the distal dendrites of CA2 neurons

AUTHORS

Katy E. Pannoni[1], Quentin S. Fischer[1], Renesa Tarannum[1,2], Mikel L. Cawley[1,2], Mayd M. Alsalman[1], Nicole Acosta[1], Chisom Ezigbo[1], Daniela V. Gil[1], Logan A. Campbell[1], Shannon Farris[1,3,4,#]

AFFILIATIONS

[1]Fralin Biomedical Research Institute at Virginia Tech Carilion, Center for Neurobiology Research, Roanoke, Virginia
[2]Graduate Program in Translational Biology, Medicine, and Health, Virginia Tech, Blacksburg, Virginia
[3]Department of Biomedical Sciences & Pathobiology, Virginia-Maryland College of Veterinary Medicine, Virginia Tech, Blacksburg, Virginia
[4]Virginia Tech Carilion School of Medicine, Roanoke, Virginia

[#]Lead author, correspondence**:** farrissl@vtc.vt.edu

KEYWORDS

Mitochondrial calcium uniporter, Hippocampal CA2, Synaptic plasticity, Mitochondrial morphology, Dendrites, Spines

ABSTRACT

Mitochondria are dynamic organelles that are morphologically and functionally diverse across different cell types and subcellular compartments in order to meet unique energy demands. In neurons, mitochondria are critical to support synapses and synaptic plasticity. However, the mechanisms regulating mitochondria in synaptic plasticity are largely unknown. The mitochondrial calcium uniporter (MCU) regulates calcium entry into the mitochondria, which in turn regulates the bioenergetics and distribution of mitochondria to active synapses. Evidence suggests that calcium influx via MCU couples neuronal activity to mitochondrial metabolism and ATP production, which would allow neurons to rapidly adapt to changing energy demands. Intriguingly, MCU is uniquely enriched in CA2 distal dendrites relative to neighboring CA1 or CA3 distal dendrites, suggesting mitochondria there are molecularly distinct. However, the functional significance of this enrichment is not clear. Synapses onto CA2 distal dendrites, unlike synapses onto CA2 proximal dendrites, readily undergo long-term potentiation (LTP), but the mechanisms underlying the different plasticity profiles are unknown. Therefore, we investigated the role of MCU in regulating dendritic mitochondria and synaptic plasticity in CA2 distal dendrites. Using a CA2-specific MCU knockout (cKO) mouse, we found that MCU is required for LTP at CA2 distal dendrite synapses. Loss of LTP correlated with a trend for decreased spine density in CA2 distal dendrites of cKO mice compared to control (CTL) mice, which was predominantly seen in immature spines Moreover, mitochondria were significantly smaller and more numerous across all dendritic layers of CA2 in cKO mice compared to CTL mice, suggesting an overall increase in mitochondrial fragmentation. Fragmented mitochondria might have functional changes, such as altered ATP production, that might explain a deficit in synaptic plasticity. Collectively, our data reveal that MCU regulates layer-specific forms of plasticity in CA2 dendrites, potentially by maintaining proper mitochondria morphology and distribution within dendrites. Differences in MCU expression across different cell types and circuits might be a general mechanism to tune the sensitivity of mitochondria to cytoplasmic calcium levels to power synaptic plasticity.

MAIN TAKE HOME POINTS

- The mitochondrial calcium uniporter regulates plasticity selectively at synapses in CA2 distal dendrites.
- The MCU-cKO induced LTP deficit at synapses in CA2 distal dendrites correlates with a trending reduction in spine density.
- Loss of MCU in CA2 results in ultrastructural changes in dendritic mitochondria that suggest an increase in mitochondrial fragmentation. These ultrastructural changes could result in functional consequences, such as decreased ATP production, that could underlie the plasticity deficit.

INTRODUCTION

Mitochondria dynamically regulate many critical cellular functions, including energy production and calcium buffering, to meet the unique demands of different cell types (Pekkurnaz & Wang, 2022; Sprenger & Langer, 2019; Fecher et al., 2019). Even within a cell, mitochondria display remarkable heterogeneity across subcellular compartments (Faitg et al., 2021; Lewis et al., 2018; Pannoni et al., 2023), which is especially critical for highly polarized cells such as neurons. The extent to which mitochondrial diversity influences cell-specific functions remains an open question. In neurons, there is growing evidence demonstrating the importance of mitochondria for synapses and plasticity (Devine and Kittler 2018; Tang and Zucker 1997; Li et al., 2004; Smith et al., 2016; Stowers et al., 2002). Mitochondria at the presynapse enhance pre-synaptic vesicle mobilization during long-term potentiation (LTP; Smith et al., 2016). Post-synaptically, loss of dendritic mitochondria leads to a loss of dendritic spines and synapses in cultured neurons (Li et al., 2004). Evidence in cultured neurons suggests that dendritic mitochondria are needed to power local translation during structural LTP at dendritic spines (Rangaraju et al., 2019). Additionally, chemically induced LTP requires a rapid burst of mitochondrial fission in cultured hippocampal neurons (Divakaruni et al., 2018). It remains unclear, however, the mechanism(s) by which mitochondria regulate synaptic plasticity and how this might vary by cell type or circuit.

The mitochondrial calcium uniporter (MCU) is a channel that allows calcium flux across the inner mitochondrial membrane into the matrix of the mitochondria (Baughman et al., 2011, Stefani et al., 2011; Chaudhuri et al., 2013), where it has potentially far reaching effects on mitochondrial form and function (Llorente-Folch et al., 2015; Zhao et al., 2015; Rizzuto et al., 2012; Wescott et al., 2019). While this has been extensively studied in pathological conditions and in culture (Qiu et al., 2013; Llorente-Folch et al., 2015; Zhao et al., 2015; Liang et al., 2014), little is known about the role mitochondrial calcium uptake plays in intact neural circuits. Recently, it's been shown that driving high frequency action potential firing in acute hippocampal or cortical slices leads to increased mitochondrial calcium uptake via MCU and an increase in NADH metabolism in the soma and somatodendritic compartment (Groten & MacVicar, 2022). Uptake of calcium into dendritic mitochondria is coincident with NMDAR-dependent synaptic activity in cortical slices (Stoler et al., 2022). In addition, chemical LTP results in a transient elevation of calcium in the mitochondrial matrix in cultured hippocampal neuron dendrites (Divakaruni et al., 2018). These studies provide a potential link between synaptic activity, mitochondrial calcium uptake and bioenergetics that could allow mitochondria to rapidly respond to increased energy demands. However, the role of MCU in postsynaptic LTP is unknown.

Previously, we showed that hippocampal area CA2, an understudied subregion of the hippocampus that is critical for social memory (Hitti and Siegelbaum 2014; Stevenson and Caldwell 2014; Dudek, Alexander, and Farris 2016) has a particularly high expression of MCU relative to neighboring hippocampal areas CA1 and CA3 (Pannoni et al., 2023; Farris et al., 2019). However, the functional significance of MCU enrichment in CA2 neurons remained unclear. In contrast to CA1 neurons, CA2 neurons are known for being resistant to tetanus-induced LTP (Zhao et al., 2007) likely due to robust calcium buffering and extrusion mechanisms (Simons et al., 2011; Carstens and Dudek, 2019). While this is the case for synapses onto the proximal dendrites of CA2, synapses onto distal dendrites of CA2 readily express LTP (Chevaleyre and Siegelbaum 2010; Dudek et al.

2016). There are not any known candidates distinguishing CA2 proximal and distal synapses that could mediate these functional differences in plasticity. We recently uncovered that the propensity for LTP in CA2 correlates with more mitochondrial mass and higher expression of MCU selectively in distal dendrites compared to proximal dendrites (Pannoni et al., 2023). The distinct enrichment of MCU in CA2 distal dendrites is not merely due to the increased mitochondrial mass there, as other mitochondrial markers, such as COX4, do not show the same level of enrichment as MCU in CA2 distal dendrites and do not differ between areas CA1 and CA2 (Pannoni et al 2023). Thus, we predicted that layer-specific enrichment of MCU in CA2 distal dendrites may be important for promoting plasticity in otherwise LTP-resistant CA2 neurons. In this paper, we examine the role of MCU in the expression of LTP, dendritic spine density, and mitochondrial ultrastructure in CA2 dendrites using a conditional KO of MCU in CA2 neurons. We hypothesize that loss of MCU in CA2 neurons will result in a dysregulated mitochondrial network, causing dendritic spine changes and deficits in synaptic plasticity. Consistent with this, we found MCU is necessary for both the induction of LTP at CA2 distal dendrite synapses and for maintaining proper mitochondrial morphology across all CA2 dendrite layers. Loss of MCU did not alter the greater mitochondrial mass in distal dendrites compared to proximal dendrites, indicating that MCU is not a driver of mitochondrial structural heterogeneity in CA2 dendrites. These data expand on the underexplored role of MCU in synaptic plasticity and the diversity of mitochondria morphology in a cell type critical for social memory. Understanding how diverse mitochondria regulate cellular functions to meet cell-type and circuit-specific needs is critical to our overall understanding of the brain in health and disease.

RESULTS

Conditional deletion of MCU in hippocampal CA2 neurons.

To examine whether MCU plays a role in the layer-specific plasticity profile of CA2, we generated a CA2-specific knock-out mouse of MCU by crossing an Amigo2-cre mouse line (Alexander et al., 2018) to an MCU $^{fl/fl}$ line (Kwong et al., 2015). Sections from adult MCU $^{fl/fl}$;Amigo2-cre negative (CTL) and MCU$^{fl/fl}$;Amigo2-cre positive (cKO) mouse brains were immunostained for MCU and CA2 neuronal marker RGS14 to validate the selective loss of MCU in CA2 neurons. On average, 88% (± 2.2, N = 7 mice) of RGS14 positive CA2 neurons express MCU in CTL mice. After postnatal MCU deletion, 10% (± 2.7, N = 8 mice) of RGS14 positive CA2 neurons express MCU (Fig. 1AB). There was a significant decrease in the number of RGS14 positive neurons that express MCU in cKO mice compared to CTL mice (Fig. 1B; CTL: 39.8 ± 2.6 neurons, cKO: 4.3 ± 1.1 neurons, two-tailed unpaired t-test, $p<0.0001$) without a difference in the total number of RGS14 positive CA2 neurons between genotypes (Fig. 1C; CTL: 45.4 ± 2.6 neurons, cKO: 39.9 ± 3.1, two-tailed unpaired t-test, $p= 0.2042$) MCU fluorescence intensity was reduced selectively in CA2 neurons (Fig. 1D; two-way ANOVA, overall effect of genotype $F (1, 52) = 22.45$, $p<0.0001$, sidak's post hoc test CTL v. cKO CA2 $p< 0.0001$), with no significant change in MCU fluorescence intensity in CA1, dentate gyrus (DG), or the neighboring cortex after MCU cKO compared to CTL (sidak's post hoc CTL v. cKO CA1, DG, CTX $p> 0.05$). Further, a decrease in MCU fluorescence intensity was seen across all layers of CA2 dendrites in the cKO compared to CTL (Fig. 1E). In the neuropil layer, MCU labeling is predominantly detected within dendrites where it localizes to the inner mitochondrial membrane as visualized with protein-retention expansion microscopy (Fig. 1F).

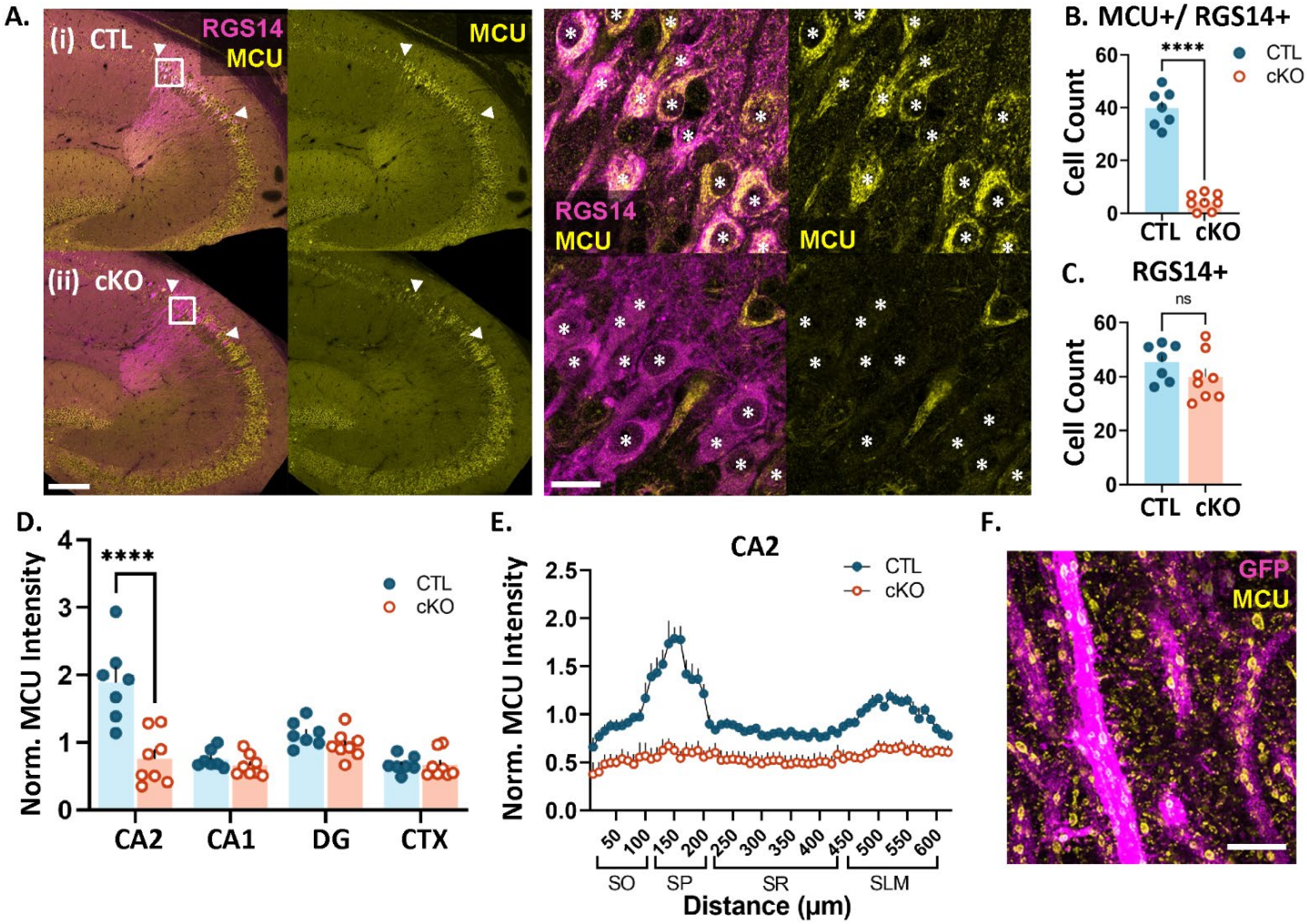

Fig. 1: MCU expression is significantly reduced in CA2 neurons of cKO mice.

A. Representative images of MCU (yellow) and RGS14 (magenta) immunostaining in CTL (i) and cKO (ii) mice. Higher magnification images of CA2 neurons are shown to the right. Asterisks indicate RGS14-positive CA2 neurons.

B. Quantification of the number of RGS14+ CA2 neurons expressing MCU (CTL: 39.8 ± 2.6 neurons, N=7 mice, cKO: 4.3 ± 1.1 neurons, N=8 mice, two-tailed unpaired t-test, $p<0.0001$)

C. The total number of RGS14-positive CA2 neurons does not differ between CTL and cKO mice (CTL: 45.4 ± 2.6 neurons, cKO: 39.9 ± 3.1, two-tailed unpaired t-test, $p= 0.2042$)

D. Comparison of MCU fluorescence intensity in CTL and cKO mice in CA2, CA1, dentate gyrus (DG) and neighboring cortex (CTX). Data were normalized to the CTL average. (two-way ANOVA, overall effect of genotype $F (1, 52) = 22.45$, $p<0.0001$; overall effect of subregion $F (3, 52) = 17.80$, $p<0.0001$, interaction $F (3, 52) = 12.74$, $p<0.0001$; sidak's post hoc test CTL v. cKO CA2 $p< 0.0001$).

E. Line plot analysis of MCU fluorescence intensity across CA2 layers in CTL and cKO mice. Data are normalized to the CA2 CTL average.

F. Representative super resolution image of MCU (yellow) in genetically labeled CA2 dendrites (magenta) using expansion microscopy. Scale = 200 μm and 25 μm (A) and 5 μm, ExM adjusted (F). ****$p<0.0001$

CA2-specific MCU cKO results in impaired LTP at distal dendrite synapses.

Next, to assess the role of MCU in the propensity of CA2 distal synapses to express LTP we recorded extracellular field potentials (FPs) from CA2 neurons in acute hippocampal slices from adult CTL and cKO mice. A stimulating electrode was placed in either the Schaffer Collateral (SC) inputs to CA2 stratum radiatum

(SR, proximal dendrites) or the Perforant Path (PP) inputs to CA2 stratum lacunosum moleculare (SLM, distal dendrites), and the recording electrode was placed in the CA2 stratum pyramidal (Fig. 2A). The recording site was marked by ejection of CFDA (a green fluorescent dye) for confirmation of placement within CA2. For recordings, a prerequisite stable 10-minute pre-conditioning baseline was obtained at 0.1Hz. This was followed by delivery of a strong tetanizing stimulation consisting of three bursts of high frequency stimulation (3 x 100 Hz for 1 second) with an interburst interval of 10 minutes. Subsequently, post-conditioning responses were recorded for a period of 60 minutes at 0.1Hz. Only one recording was made from each slice. Figure 2B shows the average normalized field potential peak amplitude evoked by stimulation of SC inputs to SR over time in the CTL (blue) and cKO (orange) conditions. The ratio of the normalized field potential peak amplitude during the last 5 minutes of post-conditioning / last 5 minutes of pre-conditioning (post/pre ratio) is plotted in Fig 2C. Consistent with observations in wildtype mice (Zhao et al., 2007), stimulation of SC inputs to the SR of CTL mice did not induce a net LTP and this did not change in cKO mice (Fig. 2BC; average post/pre ratio: CTL = 1.07 +/- 0.08, n= 7 slices from 7 mice, cKO = 1.06 +/- 0.07, n= 9 slices from 9 mice; p = 0.45, Welch's t-test). In contrast to CTL mice, where stimulation of PP inputs to SLM induced robust LTP as previously described (Chevaleyre and Siegelbaum, 2010), stimulation of PP inputs to SLM failed to induce a robust LTP in cKO mice (Fig. 2DE, average post/pre ratio: CTL= 1.54 +/- 0.19, n= 8 slices from 7 mice, cKO = 1.08 +/- 0.08 n= 7 slices from 7 mice; p = 0.03, Welch's t test). Individual time plots of normalized field potential peak amplitude over time are presented for each slice in Supplemental Figure 2. We saw a heterogeneous response to strong tetanizing stimulation with a variety of post/pre ratios (plasticity outcomes). For stimulation of SC inputs to SR in CTL and cKO slices, the majority had responses showing no change (post/pre ratios within +/-10% of baseline), while a single slice in each group exhibited LTD (post/pre ratio <90% of baseline), and 33 - 43% displayed weak LTP (post/pre ratio = 114 - 143% of baseline). This heterogeneity resulting in a net no change from baseline is consistent with previous reports with various stimulation protocols (Zhao et al 2007; McCann et al 2021). In contrast, stimulation of PP inputs to SLM in CTL slices 75% showed robust LTP (post/pre ratios = 120 - 248% of baseline), and none showed LTD; while in cKO slices 57% displayed weak LTP (post/pre ratios = 112 - 138% of baseline) and 14% displayed LTD. These results confirm layer-specific plasticity profiles in CTL CA2 and demonstrate that MCU deletion impairs the capacity of synapses in SLM to undergo robust LTP.

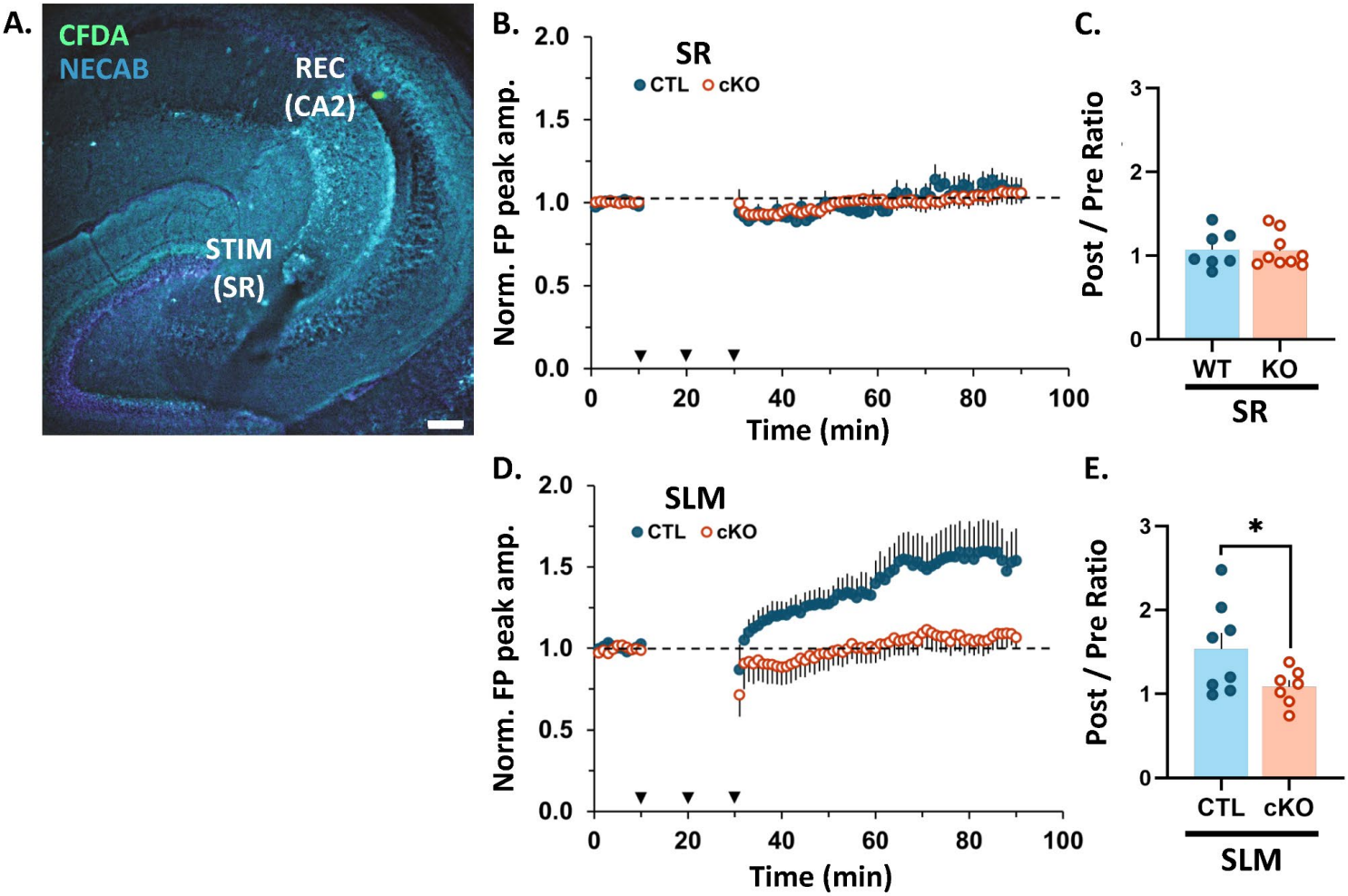

Fig. 2: CA2 MCU cKO blocks LTP in CA2 SLM, with no effect in plasticity-resistant CA2 SR.

A. Representative image of the recording and stimulating site in an acute hippocampal slice. CFDA dye (green) was pressure ejected from the recording pipette. NECAB staining (cyan) delineates CA2.

B. Average time plot of normalized field potential peak amplitudes evoked in CA2 by stimulation of SC inputs to SR of CTL (blue dots) and MCU cKO (open orange dots) slices. N = 7 CTL, 9 cKO slices. Dotted black line = baseline (all plots). Error bars = SEM (all plots).

C. Post/pre ratio of normalized field potential peak amplitudes evoked in CA2 by stimulation of SC inputs to SR of CTL and cKO slices. Welch's t-test; N = 7 CTL, 9 cKO slices.

D. Average time plot of normalized field potential peak amplitudes evoked in CA2 by stimulation of PP inputs to SLM of CTL (blue dots) and MCU cKO (open orange dots) slices. N = 8 CTL, 7 cKO slices.

E. Post/pre ratio of normalized field potential peak amplitudes evoked in CA2 by stimulation of PP inputs to SLM of CTL and cKO slices. Welch's t-test; N = 8 CTL, 7 cKO slices.

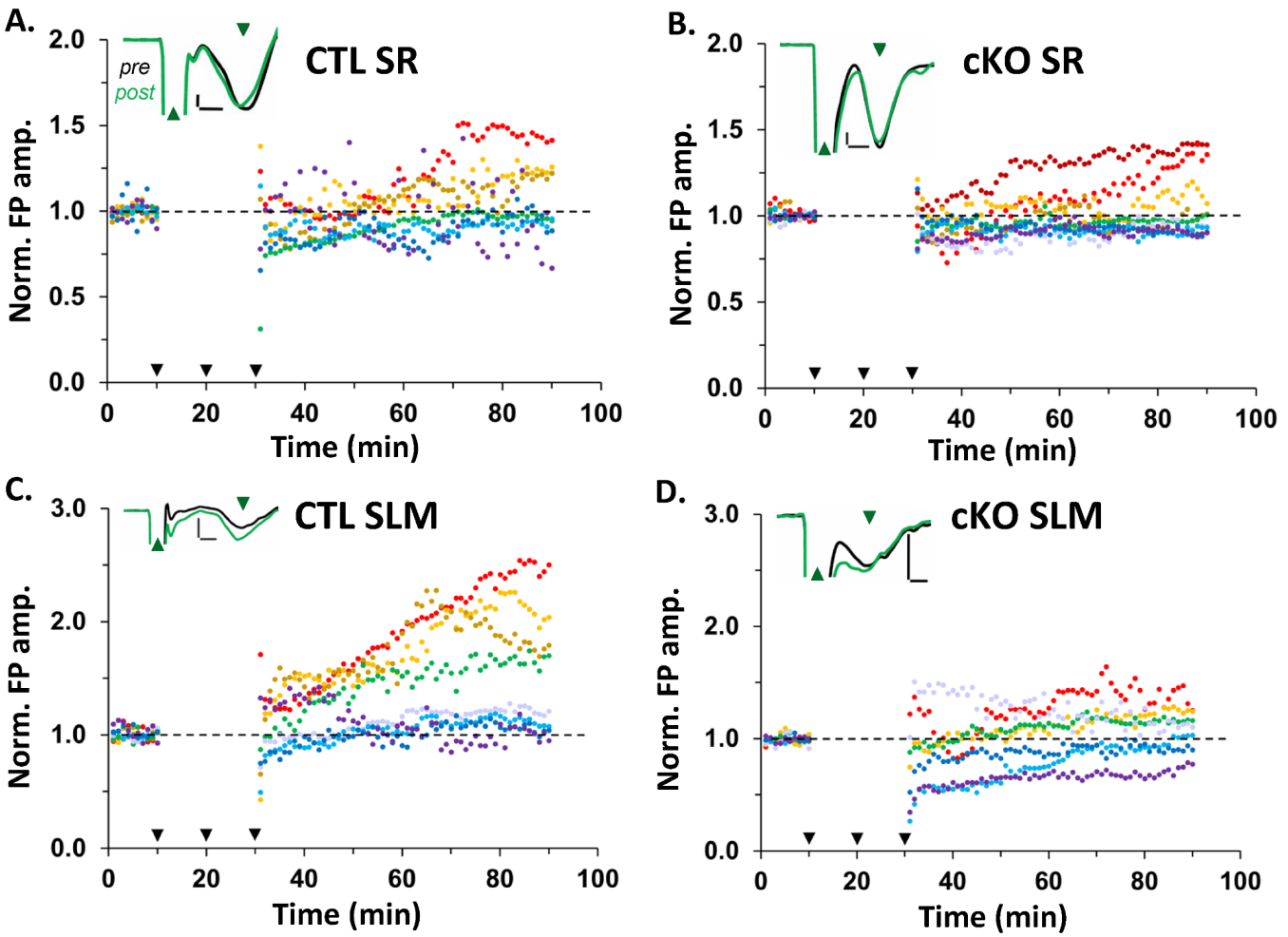

Supplemental Fig 1: Individual time plots of normalized FP peak amplitude for each region and genotype showing the heterogeneity of responses by animal.

A. Individual time plots of normalized FP peak amplitudes evoked by stimulation of SC inputs to SR of CTL slices. Individual plots are color-coded according to post/pre ratio, with progressively warmer colors representing progressively higher post/pre ratios (all panels). Black dotted line = baseline (all panels). Inset shows a representative recording of the average evoked response (up arrowhead = stimulus artifact, down arrowhead = FP) recorded during the last 5 minutes of pre-conditioning (black line) versus the last 5 minutes of post-conditioning (green line; all panels). Scale bars: 0.1mV, 0.5ms (all panels).

B. Individual time plots of normalized FP peak amplitude evoked by stimulation of SC inputs to SR of cKO slices.

C. Individual time plots of normalized FP peak amplitude evoked by stimulation of PP inputs to SLM of CTL slices.

D. Individual time plots of normalized FP peak amplitude evoked by stimulation of PP inputs to SLM of cKO slices.

A trending reduction in spine density in MCU cKO mice is driven by a decrease in immature spines

LTP involves the strengthening of existing synapses as well as growth and stabilization of new spines and synapses (Hill and Zito, 2013; Engert and Bonhoeffer, 1999; Holtmaat and Svoboda, 2009), thus we hypothesized there may be a loss of spines associated with the LTP deficit in CA2 SLM. To test this, we impregnated hippocampal sections from CTL and MCU cKO mice with Golgi-Cox staining solution (Glaser et al., 1981), a mercury-based sparse cell fill, and the density of dendritic spines in CA2 SLM was quantified. Figure 3 shows a Golgi-Cox stained hippocampal section highlighting CA2 (Fig. 3A) and representative dendrite segments from CA2 SLM of CTL (Fig. 3B) and cKO (Fig. 3C). Although not significant, there was a trend towards lower spine density in the MCU cKO compared to CTL (Fig 3D, $p = 0.052$, Welch's t-test; $N = 8$ mice per genotype). Spine density per 100 µm decreased from 97.2 (± 2.1) spines in CTL dendrites to 86.5 (±5.5) in MCU cKO dendrites, representing an 11% average decrease in density. There was significantly more animal variability in spine density for MCU cKO mice than CTL mice ($p = 0.022$, $F = 6.77$; F test for variance). In a subset of dendrites, spines were classified as immature (filopodia and thin spines) or mature (stubby, mushroom and branched spines) to assess whether the decrease in spine density was equivalent in immature and mature spines, or whether one group was more impacted (arrows in Fig. 3BC). The decrease in total spine density appears to be driven mostly by a decrease in immature spine density in cKO mice compared to CTL (Fig. 3E; average CTL 91.1 ± 6.0 spines/100 µm, cKO 80.7 ± 4.6 spines/100 µm, $p= 0.0652$, Mann Whitney one-tailed t-test) without changes in mature spine density (Fig 3F; average CTL 31.0 ± 3.32 spines/100 µm, cKO 34.9 ± 3.85 spines/100 µm, $p= 0.2316$, unpaired one-tailed t-test). The relative percentages of immature and mature spine morphologies only differed slightly between cKO and CTL (CTL immature 74.5 ± 2.8%, mature 25.6 ± 2.8%; cKO immature 70.2 ± 2.5%, mature 29.8 ± 2.5%).

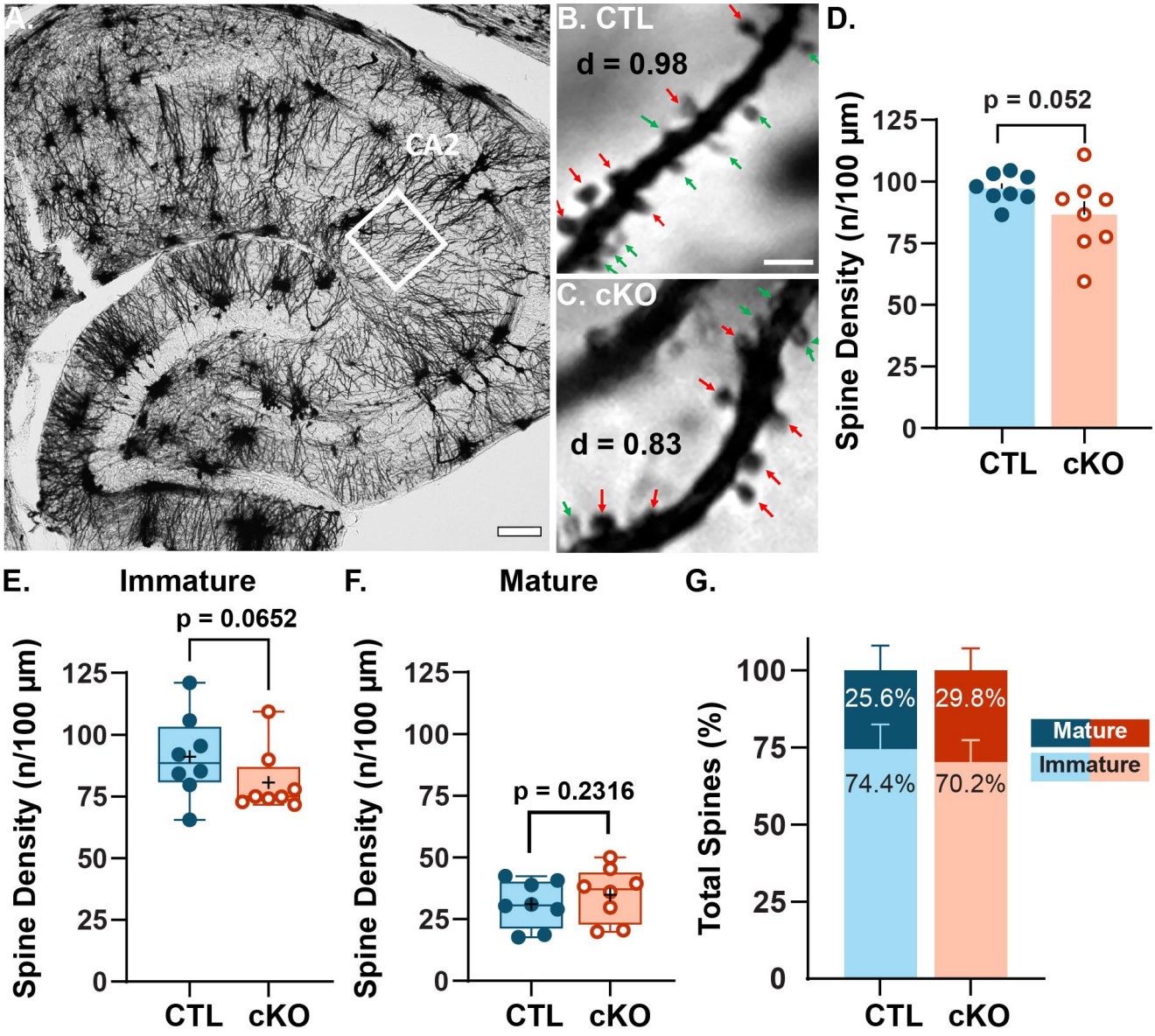

Fig. 3: MCU deletion in CA2 decreases the frequency of immature spines and increases the variability of total spine density.

A. Representative Golgi-Cox stained mouse hippocampus. The white region of interest (ROI) captures CA2 SLM dendrites. Scale = 100 µm.

B-C. Representative images of dendritic spines in CA2 SLM from CTL and MCU cKO mice, respectively. Scale = 2 µm. Immature spine = green, mature spine = red, density (d) = number of spine / length of dendrite

D. Quantification of average spine density in the CA2 SLM of CTL (blue, closed) and MCU cKO (orange, open) mice. The reduction in SLM spine density in MCU cKO is not significant but is trending compared to CTL (p=0.052, Welch's t-test; N = 8 mice per genotype). However, we note that the significance testing was impacted by the increase in variability per animal in MCU cKO mice compared to CTL (p = 0.022, F = 6.77; F test for variance).

E. Box plot showing immature spine density per animal in CTL and MCU cKO mice. (p= 0.0652, Mann Whitney, one-tailed t-test, N=8 mice per genotype) Immature spines consisted of combined counts for filopodia and thin shaped spines. These data did not have a normal distribution. □ = average spine density

F. Box plot showing mature spine density per animal in CTL and MCU cKO mice. (p= 0.2316, unpaired one-tailed t-test, N=8 mice per genotype). Note that mature spines consisted of combined counts for stubby, mushroom, and branched shaped spines. □ = average spine density

G. Bar plot of the distribution of mature and immature spine morphologies in CTL and MCU cKO mice represented as percent of the total spine count.

CA2 MCU cKO alters the morphology and mitochondrial content of dendritic mitochondria.
Studies have shown the importance of mitochondria both pre- and post-synaptically to support synaptic function and plasticity (Li et al., 2004, Stowers et al., 2002; Smith et al., 2016; Rangaraju et al., 2019). We previously showed that the propensity for LTP at CA2 distal dendrite synapses corresponds with a layer-specific enrichment of MCU and larger mitochondria relative to the other dendritic layers (Pannoni et al., 2023), which in theory could produce more ATP (Lewis et al., 2018). Calcium influx into mitochondria regulates both mitochondrial bioenergetics and the balance of fission / fusion (Llorente-Folch et al., 2015; Zhao et al., 2015), thus we hypothesized that MCU deletion may lead to changes in mitochondrial ultrastructure that could explain a plasticity deficit in CA2.

To look at changes in mitochondrial morphology after MCU deletion, we compared mitochondrial ultrastructure in scanning electron microscopy images from CTL and cKO mice. We acquired 150 x 150 μm^2 regions of interest (ROIs) from CA2 stratum oriens (SO), SR and SLM of each genotype at 2 nm resolution (Fig. 4A). A deep learning AI was used to selectively segment dendritic mitochondria in a subset of image tiles from each ROI (Biodock, 2023). Representative segmented electron micrographs for each dendritic layer for CTL and cKO mice are shown in Figure 4B-C. A total area of 155,200 μm^2 was analyzed with the AI over 2 days. The AI correctly identified an estimated 92.2% of dendritic mitochondria, with an error rate of 2 errors / 100 μm^2 area.

In CTL mice, we noted mitochondrial structural heterogeneity across CA2 dendritic layers. Mitochondria in SO of CTL mice were uniquely rounded relative to SR and SLM, with an aspect ratio closer to 1 (Supplemental Fig. 3B; Two-way ANOVA with non-parametric post hoc; Aspect Ratio SO vs SR: $p < 0.0001$; SO vs SLM: $p < 0.0001$; N SO = 2353, SR = 2904, SLM = 5236 mitos). We confirmed our previous findings based on manual segmentation that mitochondria in SLM of CTL CA2 are significantly larger in area than mitochondria in SR (supplemental Fig. 3C; Area SR vs SLM: $p < 0.0001$) (see Panoni et al., 2023). In CA2 SLM, the distance between neighboring mitochondria was significantly less than mitochondria in SO or SR (supplemental Fig 3D; NN Distance SR vs SLM: $p < 0.0001$; SO vs SLM: $p < 0.0001$). Mitochondria were also longer in CA2 SLM (supplemental Fig 3E; Feret's Diameter SR vs SLM: $p < 0.0001$; SO vs SLM: $p < 0.0001$), and there was greater overall mitochondrial content, as measured by mitochondrial count and total mitochondrial area per 100 μm^2 (Supplemental Fig. 3F, Count SR vs SLM: $p < 0.0001$; SO vs SLM: $p < 0.0001$; Total Area SR vs SLM: $p < 0.0001$; SO vs SLM: $p < 0.0001$; N CTL SO = 223, SR = 279, SLM = 260). This data confirms that the AI can detect the established morphological diversity of mitochondria across the dendritic layers of CA2. Mitochondria in the proximal and distal dendrites are separated by their mass, diameter and overall content (Supplemental Fig. 3F), whereas mitochondria in the basal dendrites are separated mostly by their aspect ratio (Supplemental Fig. 3B).

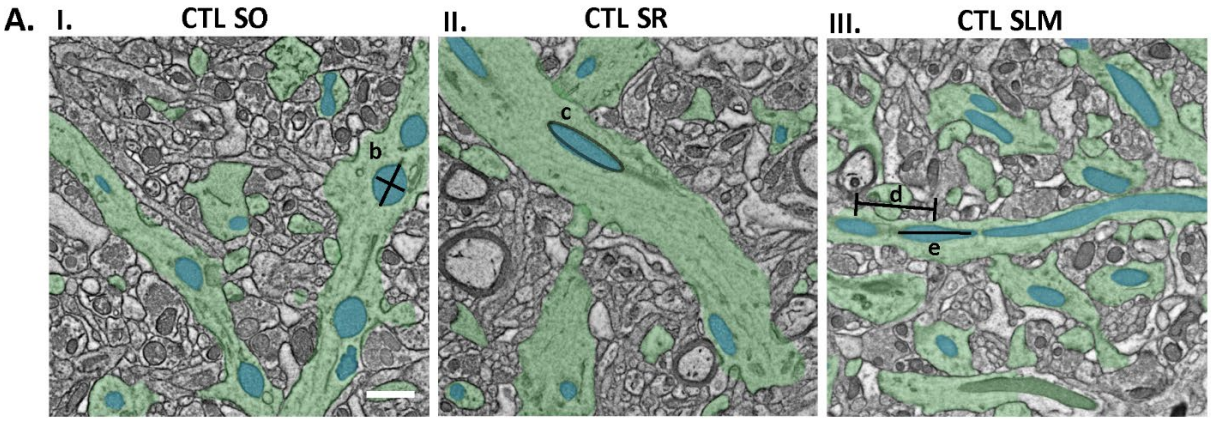

b. Aspect Ratio c. Area d. Nearest Neighbor Distance e. Feret's Diameter

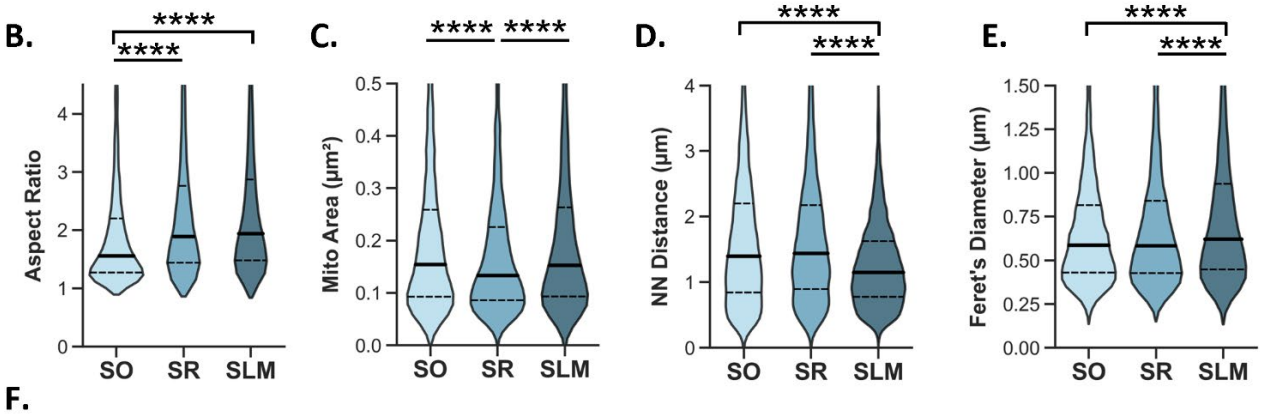

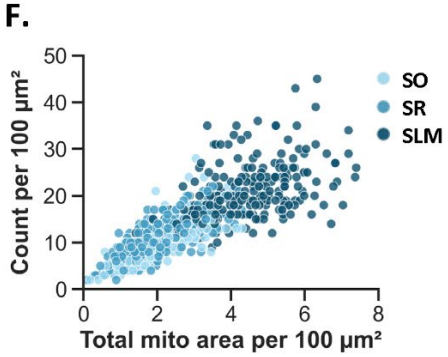

Supplemental Fig. 2: Morphometrics separate mitochondria into distinct populations within dendritic layers of wild-type CA2.

A. Representative SEM images showing dendritic mitochondria (blue) and dendrites (green) in CA2 SO, SR and SLM of CTL mice. Non-dendritic mitochondria are not labeled. Examples of the measured metrics are illustrated. Mitochondria aspect ratio was unique in SO (i), mitochondria area was unique in SR (ii), and distance to nearest neighbor and Feret's diameter were unique in SLM (iii). Scale bar = 1 μm.

B. Violin plots of mitochondrial aspect ratio in CTL CA2 SO, SR, and SLM. Overall effect of layer was significant (two-way ANOVA, $F(2, 23653) = 203.19$, $p < 0.0001$; SO n = 2353, SR n = 2904, SLM n = 5236 mitochondria from 3 CTL mice). Mann Whitney post hoc tests and Sidak's correction comparing layers are shown on the plot. See Fig. 4 for overall effect of genotype and pairwise comparisons. For all violin plots, solid line = median; dashed line = upper and lower quartiles.

C. Violin plots of individual mitochondria area in the same dataset as in (B). Overall effect of layer was significant (two-way ANOVA, $F(2, 23653) = 131.67$, $p < 0.0001$). Mann Whitney post hoc tests and Sidak's correction comparing layers are shown on the plot.

D. Violin plots of mitochondria nearest neighbor distance in the same dataset as in (B). Overall effect of layer was significant (Two-way ANOVA, $F(2, 23653) = 570.00$, $p < 0.0001$). Mann Whitney post hoc tests and Sidak's correction comparing layers are shown on the plot.

E. Violin plots of mitochondria Feret's diameter in the same dataset as in (B). Overall effect of layer was significant (two-way ANOVA, $F(2, 23653) = 162.55$, $p < 0.0001$). Mann Whitney post hoc tests and Sidak's correction comparing layers are shown on the plot.

F. A correlation plot comparing mitochondrial count and total mitochondrial area per 100 μm^2 image tile in CA2 SO (light blue), SR (medium blue), and SLM (dark blue). Overall effect of layer was significant for both mitochondria count (two-way ANOVA; $F(2, 1551) = 590.35$, $p < 0.0001$) and total mitochondria area (two-way ANOVA; $F(2, 1551) = 976.34$, $p < 0.0001$; SO n = 223, SR n = 279, SLM n = 260, n = 100 μm^2 tiles). Mitochondria in SLM are more numerous and larger than mitochondria in SO and SR.

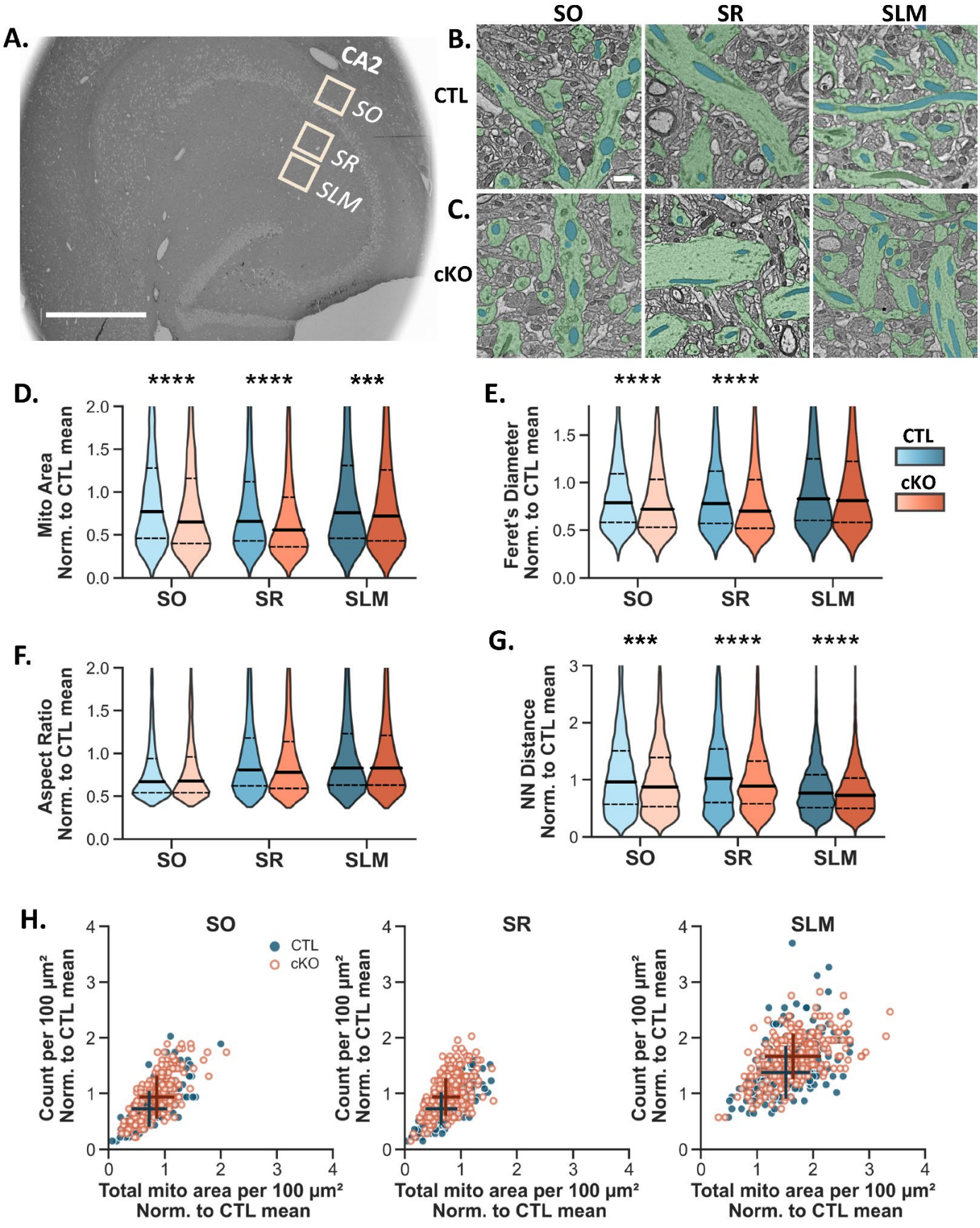

Figure 4: Dendritic mitochondria in MCU cKO mice are smaller and more numerous than CTL mice.

A. Representative scanning electron microscopy (SEM) overview image of a horizontal hippocampal section with the large ROIs representing the sampling areas from CA2 SO, SR and SLM that were quantified. Scale = 600 µm.

B. Representative SEM images from CA2 SO, SR, and SLM of the CTL group, showing dendritic mitochondria (blue) and dendrites (green). Scale = 1 μm for B-C

C. Representative SEM images from CA2 SO, SR and SLM of the MCU cKO group.

D. Violin plots of individual mitochondrial area in 100 μm^2 image tiles from CA2 SO, SR and SLM in CTL (blue) and cKO mice (orange). All plots were normalized to the overall mean of the CTL. Two-way ANOVA, significant overall effect of genotype $F(1, 23653) = 49.06$, $p < 0.0001$; significant overall effect of layer $F(2, 23653) = 131.67$, $p < 0.0001$; interaction $F(2, 7) = 7.04$, $p < 0.001$; Mann Whitney post hoc tests comparing genotypes are shown on the plot; CTL SO n = 2353, CTL SR n = 2904, CTL SLM n = 5236. cKO SO n = 2860, cKO SR = 4007, cKO SLM = 6299, n = mitochondria). Solid line = median; dashed line = upper and lower quartiles.

E. Violin plots of mitochondria Feret's diameter normalized to the overall mean of the CTL from the same dataset in (D). Two-way ANOVA, significant overall effect of genotype $F(1, 23653) = 25.47$, $p < 0.0001$; significant overall effect of layer $F(2, 23653) = 162.55$, $p < 0.0001$; interaction $F(2, 23653) = 4.15$, $p < 0.05$; Mann Whitney post hoc tests comparing genotypes are shown on the plot.

F. Violin plots of mitochondria aspect ratio normalized to the overall mean of the CTL from the same dataset in (D). Two-way ANOVA, significant overall effect of layer $F(2, 23653) = 203.19$, $p < 0.0001$ but no overall effect of genotype $F(1, 23653) = 0.566$, $p > 0.05$. See Supplemental Fig 2 for CTL layer pairwise comparisons.

G. Violin plots of mitochondria nearest neighbor distance normalized to the overall mean of the CTL from the same dataset in (D). Two-way ANOVA, significant overall effect of genotype $F(1, 23653) = 109.63$, $p < 0.0001$; significant overall effect of layer $F(2, 23653) = 570.00$, $p < 0.0001$; interaction $F(2, 23653) = 14.83$, $p < 0.0001$; Mann Whitney post hoc tests comparing genotypes are shown on the plot.

H. A correlation plot comparing mitochondrial count and total mitochondrial area per 100 μm^2 image tile in CA2 SO, SR, and SLM in CTL (closed blue dots) and MCU cKO (open orange dots). Mitochondria count and total mitochondria area were separately normalized to the overall mean of the CTL. Overall effect of genotype was significant for count (two-way ANOVA, overall effect of genotype $F(1, 1551) = 105.47$, $p < 0.0001$; significant overall effect of layer $F(2, 1551) = 590.35$, $p < 0.0001$, CTL SO n = 223, CTL SR n = 279, CTL SLM n = 260. cKO SO n = 218, cKO SR = 298, cKO SLM = 279, n = 100 μm^2 tiles) and total area (two-way ANOVA, overall effect of genotype $F(1, 1551) = 27.06$, $p < 0.0001$; significant overall effect of layer $F(2, 1551) = 976.34$, $p < 0.0001$). The cross indicates the median of the respective group with horizontal and vertical lines indicating the standard deviation for each axis.

To determine whether loss of MCU affects mitochondrial ultrastructure, we compared the dendritic mitochondria morphology in each layer in CTL and MCU cKO mice. In MCU cKO mice, individual mitochondria were significantly smaller (Fig. 4D; two-way ANOVA with sidak's post hoc test; effect of genotype $p < 0.0001$; N CTL SO = 2353, SR = 2904, SLM = 5236 mitos, cKO SO = 2860, SR = 4007, SLM = 6299 mitos) and shorter in the long axis (Feret's) diameter (Fig 4E; effect of genotype $p < 0.0001$) across all dendritic layers compared to CTL mice, with no changes in aspect ratio (Fig. 4F, effect of genotype $p = 0.566$). This indicates that mitochondria are smaller in both dimensions in cKO relative to CTL. Unexpectedly, there was a decrease in nearest neighbor distance (Fig. 4G; two-way ANOVA with sidak's post hoc test; effect of genotype $p < 0.0001$; N CTL SO = 223, SR = 279, SLM = 260, cKO SO = 223, SR = 279, SLM = 260) and an increase in mitochondrial count per 100 μm^2 in all dendritic layers (Fig. 4H; effect of genotype $p < 0.0001$). A decrease in individual mitochondria area in combination with an increase in mitochondria count suggests that MCU cKO causes an increase in mitochondria fragmentation. The increase in mitochondrial count was greatest in SLM (Median number of mitochondria per 100 μm^2: CTL SLM: 19 ± 0.24, cKO SLM: 23 ± 0.27; CTL SR: 10 ± 0.41, cKO SR: 13 ± 0.34; CTL SO: 10 ± 0.30, cKO SO: 13 ± 0.36; Fig 4H) and appears to be driving an increase in overall mitochondrial content after MCU cKO (Fig. 4H). Taken together, our data suggest that mitochondrial fragmentation is increased after MCU cKO in CA2, and this effect was seen across all dendritic layers.

Strikingly, the relative differences in mitochondria size and overall content across dendritic layers were not altered in MCU cKO mice compared to CTL. Although we saw no obvious signs of damaged or unhealthy mitochondria in the MCU KO condition at the ultrastructural level, there may be functional changes or deficits that would not be observed in EM micrographs, such as decreased metabolism and ATP production. We did note several examples where the distribution of mitochondria within the dendrites changed from a linear network with mitochondria oriented end to end in the control dendrites, to a stacked distribution resembling multiple lanes of traffic in many cKO dendrites (see Fig. 4C), which is supported by a decrease in the nearest neighbor distance (Fig 4G). It is not yet clear the functional significance, if any, of this change.

DISCUSSION

In the present study, we examined the role of MCU in LTP, dendritic spine density and mitochondrial ultrastructure in CA2 dendrites using a CA2-specific MCU knockout mouse line. We found that MCU is necessary for LTP at CA2 distal synapses, but MCU loss does not alter the lack of plasticity at CA2 proximal synapses. The LTP deficit at synapses in CA2 distal dendrites of MCU cKO correlated with a trending decrease in overall spine density compared to CTL distal dendrites, which was predominantly accounted for by fewer immature spines. Looking at the effect of MCU cKO on dendritic mitochondria ultrastructure in CA2, mitochondria were smaller, more numerous and closer together in MCU cKO mice, suggesting there is more mitochondrial fragmentation. These ultrastructural changes were seen across all dendritic layers of CA2 to different extents. Further, the loss of MCU did not alter the layer-specific differences in mitochondria morphology across CA2 dendrites, suggesting that the asymmetrical expression of MCU across wild-type CA2 dendritic layers is not necessary to establish or maintain the structural diversity of mitochondria. However, MCU enrichment in CA2 SLM may still confer unique functional properties to mitochondria that are necessary for LTP at those synapses.

A role for MCU in the propensity of CA2 distal synapses to undergo LTP

Our results demonstrate a role for MCU in LTP at distal synapses in CA2. Given that many features of CA2 neurons are unique, it is not clear whether our results are specific to CA2 or could be generalized to other cell types. CA2 neurons highly express a number of genes that act as molecular brakes on plasticity (Carstens and Dudek 2019), and some of those mechanisms involve restricting calcium signaling (Evans et al., 2018; Simons et al., 2011). LTP is highly dependent on calcium influx into the post-synapse and resulting downstream signaling cascades (Nicoll, 2017). Calcium transients in the post-synapse bidirectionally regulate synaptic plasticity in CA1 neurons, with large calcium spikes inducing LTP while prolonged low calcium spikes induce long-term depression (Cormier et al., 2021). CA2 neurons have a significantly faster rate of calcium extrusion than CA1 and CA3 neurons, as well as an increased calcium buffering capacity, which mitochondria may contribute to (Simons et al., 2009). The same study also showed that CA2 neurons have the lowest endogenous free calcium at rest and that increasing intracellular calcium levels permits LTP at the typically resistant CA2 SR synapses. Because none of the identified brakes on CA2 plasticity are spatially restricted to SR, it is possible that SLM harbors additional mechanisms to overcome these molecular brakes and express LTP. MCU could fulfill this role , as MCU expression is enriched in SLM compared to SR and one function of MCU is to couple neuronal activity to energy metabolism by decoding intracellular calcium levels (Groten and MacVicar, 2022, Stoler et al., 2022; Bas-Orth et al., 2020). We speculate that the enrichment of MCU at CA2 distal dendrites may promote LTP by enhancing the sensitivity of mitochondria to changes in cytoplasmic calcium, potentially to couple it to ATP production. Thus, it is possible that MCU plays a general role in proper LTP expression in other cell-types by boosting ATP, but differential MCU expression may tune the mitochondrial response to the unique calcium dynamics of the cell or circuit. It was recently shown that MCU is required for action potential evoked production of NADH by mitochondria (Groten and MacVicar, 2022). Further, high-frequency action potential firing causes MCU-dependent mitochondrial calcium uptake that differs between the hippocampus and cortex (Groten and MacVicar, 2022), suggesting that variability in the coupling

of activity and mitochondrial calcium uptake due to differences in MCU expression could be a mechanism for tuning energy production to unique cell-type specific properties. While these data focus on the role of MCU in powering sustained action potential firing, others have shown mitochondrial calcium uptake occurs with the coincidence of pre- and postsynaptic activity in dendrites (Stoler et al., 2022). Alternatively, it is possible that MCU may differentially impact plasticity depending on the cell types and forms of plasticity involved. Consistent with this idea, global MCU haploinsufficiency enhanced presynaptic LTP at DG-CA3 synapses in hippocampal slices (Devine et al., 2022). Specifically, clearance of presynaptic calcium by mitochondria was reduced in MCU+/- mice, increasing vesicle release probability, despite reduced ATP (Devine et al., 2022). This contrasting finding could be explained by different roles for MCU pre- versus post-synaptically, or due to differences in the effects of cell-specific homozygous MCU deletion mice versus global haploinsufficient MCU mice. While emerging evidence supports a role for MCU in regulating energy production and calcium buffering in both pre (Ashrafi et al., 2020) and post (MacVicar et al., 2022; Stoler et al., 2021) synaptic functions, further studies are needed to resolve its impact on specific cell types and circuits as well as the underlying mechanisms linking it to plasticity.

MCU loss results in changes to spine morphology

We detected a ~10% decrease in spine density in MCU cKO mice that could contribute to the deficit in LTP. This non-significant decrease is largely explained by a loss of immature spines while mature spines were relatively stable when compared to CTL. This suggests that immature spines may be more vulnerable to loss of MCU. It is widely accepted that mushroom spines are relatively more stable than filopodia and immature spine types (Kasai et al., 2003). Notably, we found that ~75% of spines in CA2 SLM were immature. This is much higher than estimates from others that ~20% of spines are immature in adult brains (Berry and Nedivi, 2017), highlighting that CA2 SLM has a particularly high proportion of immature spines, or that our criteria for manually categorizing spine shape differs. However, the LTP deficit may also be due to non-structural changes in dendritic spines. Spines in CA2 SLM receive input from entorhinal cortical layer II neurons (ECII) and activity from the lateral ECII to CA2 is required for social recognition memory (Lopez-Rojas et al. 2021). Given the LTP and spine deficits we uncovered in SLM, further studies are warranted to test whether MCU cKO in CA2 has an effect on social recognition memory.

Mitochondrial fragmentation due to MCU deletion

Mitochondria are highly dynamic organelles that are shaped by two opposing forces: fission and fusion. Mitochondrial fission, the division of mitochondria to make new or recycle damaged mitochondria, is mediated by the phosphorylation of dynamin-related protein 1 (DRP1; Zheng et al., 2017). Whereas fusion of mitochondria is mediated by optic atrophy 1 (OPA1) and mitofusins (Legros et al., 2002, Cipolat et al., 2004). The balance of these forces determines mitochondrial form, which is intimately linked to bioenergetics. For example, it's been shown that larger axonal mitochondria in cortical neurons can produce more ATP (Lewis et al., 2018). Fragmented mitochondria could result in functional consequences, such as decreased ATP production, altered ROS generation or calcium-induced calcium release, that might underlie a plasticity deficit. There are multiple potential causes of mitochondrial fragmentation after MCU deletion. In cultured rat hippocampal dendrites, mitochondrial fission is rapidly triggered by chemical LTP (Divakaruni et al., 2018). This mitochondrial fission requires CaMKII and DRP1 and precedes mitochondrial calcium uptake (Divakaruni et al., 2018). Expression of dominant negative forms of DRP1 blocks mitochondrial fission and LTP in culture and in CA1 of acute hippocampal slices (Divakaruni et al., 2018). Therefore, loss of MCU may elevate cytoplasmic calcium levels and lead to aberrant activation of DRP1 that could, in theory, result in more fragmented mitochondria. The effect of MCU loss on mitochondrial number was greatest in SLM, suggesting the mitochondria might be more fragmented in SLM relative to SO or SR in MCU cKO mice– although, it did not scale proportionally with a greater decrease in individual mitochondria area or diameter in SLM.

On the other hand, inhibition of MCU has been shown to prevent mitochondrial fission and fragmentation in cultured hippocampal neurons during ischemia (Zhao et al., 2015). MCU has also been shown

to mediate mitochondrial fission in rat cortex (Liang et al., 2014). Although these studies are in contrast to our findings that loss of MCU results in an increase in mitochondria fragmentation in CA2, most have looked at MCU loss in the context of injury and disease. Endogenous MCU expression is also highly variable across cell types, suggesting different cell types may have different sensitivities to MCU-induced mitochondrial fragmentation and cell death (Granatiero et al., 2019) . It is also possible that the fragmentation we found is not due to increased fission mediated by DRP1, but instead an impairment in fusion, or a result of unhealthy or damaged mitochondria. Lewis et al showed that a loss of synapses correlated with increased local mitochondrial fission and ULK2-dependent mitophagy in CA1 apical dendrites in an Alzheimer's disease model (Lewis et al., 2022). However, we did not observe a loss of mitochondrial biomass and the mitochondria in our MCU cKO mice appear ultrastructurally normal in electron micrographs. Even so, the mitochondrial structural changes we observed (ie. fragmentation) may indicate functional changes that would not necessarily be observed in electron micrographs.

Altered mitochondrial distribution in dendrites due to MCU deletion

Generally, the distribution of mitochondria strongly correlates with predicted energy usage, which in neurons is highest at the synapse (Harris et al., 2012). In this study as and our previous study, we found that CA2 distal dendrites (SLM) harbor more mitochondrial mass than proximal (SR) and basal (SO) dendrites, suggesting that synapses in distal dendrites require more energy. We reasoned that this might be due to the propensity of CA2 SLM synapses to undergo LTP. However, in MCU cKO mice that fail to produce robust LTP at SLM synapses, the relative increased mitochondrial mass in SLM remains. Indeed, the structural heterogeneity across dendritic layers in MCU cKO was similar to CTL, except that mitochondria were overall smaller and more numerous across all dendritic layers in MCU cKO mice. Interestingly, mitochondrial diameter did not decrease in SLM as it did in SO and SR of cKO mice. However, the relative ultrastructural differences across dendritic layers were unchanged. This indicates that MCU expression is not related to the differences in mitochondrial structure across CA2 dendrites. Similar heterogeneity has also been reported in CA1 neurons (Virga et al., 2023). Recently, layer-specific activity-driven differences in AMPK and CAMKK2, which regulate fission/fusion factors, were shown to contribute to the differences in mitochondria shape, in particular for CA1 basal and proximal layers (Virga et al., 2023). However, whether there are similar fission/fusion differences in CA2 dendrites given their layer-specific synaptic plasticity profiles remains to be explored.

We also found that the distances between neighboring mitochondria was reduced in MCU cKO mice across CA2 dendrites, suggesting that the distribution of mitochondria may be altered. The distribution of mitochondria in dendrites is critical for synaptic function (Li et al., 2004). While mitochondria are rarely seen inside dendritic spines in mature neurons, spines are seen to contain Endoplasmic Reticulum (ER) associated with nearby mitochondria in electron micrographs from CA1, CA3, and dentate gyrus (DG) of ground squirrels (Popov et al., 2005). Mitochondria are known to form close connections with ER (< 200 nm) at zones called "mitochondrial associated membranes" (MAM), which allow for communication and the transfer of proteins, ions and metabolites between mitochondria and ER (Rizzuto et al., 2012; Giorgi et al., 2019). An estimated 20% of mitochondrial surface is in close apposition to the ER in living HeLa cells (Rizzuto et al., 1998). It is thought that calcium release from the ER at MAMs is taken up into the mitochondria via MCU and voltage-dependent anion channels on the outer mitochondrial membrane (Rizzuto et al., 2012). MCU deletion could potentially alter these MAM domains and disrupt the ER-mitochondria connection, which would likely have functional consequences at the synapse. This could be one possible explanation for the altered distribution of mitochondria we found within CA2 SLM dendrites in MCU cKO mice, including a decrease in nearest neighbor distance and a "stacked" orientation of the mitochondria in some dendrites. The resolution was not high enough in our SEM dataset to segment or quantify ER-Mitochondria contacts. Mitochondria are also seen to form filamentous reticular networks between other mitochondria in dendrites from CA1, CA3 and dentate gyrus (Popov et al., 2005), which could also be disrupted by MCU cKO. While this has not been studied in CA2 of the hippocampus, we observed what appear to be thin connections between dendritic mitochondria at both the electron microscopy and immunohistological level.

Limitations

We acknowledge that the present study has limitations. We have not shown here a direct causal relationship between changes in mitochondria morphology and LTP or spine changes, merely a correlation. It's possible these effects occur by different, potentially independent, mechanisms. Further studies will be needed to determine whether MCU deletion in CA2 negatively impacts mitochondrial metabolism; however this is technically difficult to measure in situ in such a small subregion in a layer specific manner. In addition, because the cre-dependent recombination of MCU occurs sometime between the age of postnatal (p)4-14, there is the potential for compensation to occur. Compensation could involve MCU-independent methods of calcium entry into the mitochondria; which have been observed in astrocytic mitochondria (Huntington & Srinivasan, 2021); however, given that MCU loss or inhibition by Ru360 blocks calcium uptake in mitochondria from heart, liver and neurons (Pan et al., 2013; Hamilton et al., 2018), this is unlikely to be the case. Compensation could also involve a shift in mitochondrial respiration to rely more on the malate-aspartate shuttle (MAS). Studies show there is a reversible inhibition of MAS by MCU activation, caused by increased calcium levels in the mitochondrial matrix of isolated mitochondria from brain, liver, and heart (Contreras and Satrústegui, 2009; Satrústegui and Bak, 2015), suggesting that a metabolic switch could be made to compensate when mitochondrial calcium levels are low.

Another potential limitation is that mitochondria ultrastructure in 2D SEM images may not provide a full picture of the volume and shape of the mitochondria. The mitochondria count reported is not a true count of individual mitochondria, but a count of mitochondrial segments in the image. This could artificially inflate the mitochondria count particularly in CA2 SLM, where mitochondria are longer and there is more dendritic branching, both of which could result in individual mitochondria going in/out of plane more frequently and being counted as multiple mitochondria. However, it is unlikely this would be different across cKO and CTL groups. In addition, the AI did occasionally miss dendritic mitochondria (~ 1 dendritic mito missed per 100 μm^2) and, less commonly, segment non-dendritic mitochondria (2.6% of segmentented mitochondria). Importantly, the AI performed similarly across cKO and CTL images (Error rate per 100 μm^2 : 2 in cKO; 1.7 in CTL), which allows us to confidently compare dendritic mitochondria across cKO and CTL mice. Others have made comparisons of 3D mitochondrial ultrastructure in SEM across nucleus accumbens (NA), CA1, cortex and dorsal cochlear nucleus (DCN) (Delgado et al., 2019). Consistent with these results, we observed that dendritic mitochondria were large and filamentous compared to axonal mitochondria in our 2D SEM dataset (Supplemental Fig 2A). It is important to emphasize that our statistical measurements overestimate the significance of detected effects by treating individual mitochondria as statistically independent. Other EM studies similarly analyze mitochondrial ultrastructure at the level of individual mitochondria (Smith et al., 2016; Faitg et al., 2021), however, they typically do not have thousands of mitochondria per sample. Thus, while the AI analysis is powerful in that we could analyze so many mitochondria, the statistical measurements should be interpreted with this in mind.

Combined, our results demonstrate a role for MCU in regulating layer-specific plasticity in CA2 distal dendrites and for maintaining proper spine and mitochondrial morphology and distribution in dendrites but MCU is dispensable for mitochondrial structural diversity across CA2 dendrites. We speculate that MCU may generally function postsynaptically to decode cytoplasmic calcium signals to boost metabolic output leading to long lasting changes in synaptic efficacy and that differences in postsynaptic MCU expression may reflect a general mechanism to tune ATP production in different calcium contexts.

METHODS

Animals

All experiments were performed on adult (8-16 week old unless otherwise noted) male and female mice on a C57BL/6J background. MCU CTL and cKO mice were generated by crossing a CA2-specific Amigo2-cre mouse line (Alexander et al., 2018) to an MCU $^{fl/fl}$ line (Kwong et al., 2015). Resulting heterozygous mice were crossed to produce MCU$^{fl/fl}$;Amigo2-cre positive and negative mice, which were then bred together to produce the experimental animals. Genotypes were confirmed for the MCU floxed or WT allele and the presence or absence of cre using transnetyx genotyping service. The Amigo2-cre line has been validated for conditional deletion of knocked in floxed alleles, demonstrating cre recombination occurring between postnatal ages p4 and p14 (McCan et al 2019 PMID: 31745235). Mice were group-housed when possible under a 12:12 light/dark cycle with access to food and water ad libitum. All procedures were approved by the Animal Care and Use Committee of Virginia Tech.

Electrophysiology: In vitro brain slice preparation and recording

Experiments were performed on litters at ages 10-20 weeks with the experimenter blind to genotype. Cutting and recording solutions were made as described in Helton et al 2019. Mice were deeply anesthetized with 4% isoflurane and decapitated. The brain was rapidly removed and cooled for 2 min in ice-cold cutting solution containing (in mM): 10 NaCl, 2.5 KCl, 10 D-(+)-glucose, 25 $NaHCO_3$, 1.25 NaH_2PO_4, 2 sodium pyruvate, 195 sucrose, 7 $MgCl_2$, 0.5 $CaCl_2$, and saturated with 95% O_2/5% CO_2 with a final pH of 7.4. Horizontal slices of the hippocampus were cut at 300 µm using a vibratome (VT1000S, Lecia) and placed in artificial cerebrospinal fluid (ACSF) containing (in mM): 125 NaCl, 2.5 KCl, 1.25 NaH_2PO_4, 25 $NaHCO_3$, 20 D-(+)-glucose, 2 Na-pyruvate, 2 $MgCl_2$, 2 $CaCl_2$, and saturated with 95% O_2/5% CO_2 with a final pH of 7.4. Slices were incubated in ACSF at 33±1^{o}C for 20 min and then at room temperature for > 40 min prior to recording.

For recording, slices were transferred to a submerged recording chamber perfused continuously with 3 ml/min of oxygenated ACSF at 33 ± 1^{o}C. CA2 pyramidal neurons were visualized using a Zeiss microscope (Axio Examiner.D1; Zeiss) equipped with a W Plan-Apochromat 40x water immersion lens configured for DODT gradient contrast (DGC) microscopy. A stimulating electrode (model #30213; FHC inc.) was placed in either the SC to stimulate inputs to the SR, or PP to stimulate inputs to the SLM. For recording, glass micropipettes (O.D. 1.5 mm, I.D. 1.12 mm; A-M Systems) were pulled on a vertical puller (PC-10, Narishige) to make field potential (FP) pipettes (1.2 ± 0.5 MΩ). FP pipettes were filled with ACSF and placed in the stratum pyramidal of CA2. CFDA-SE (an amine-reactive cell-permeable fluorescent green dye; Thermo-Fisher) was added to the pipette solution and pressure ejected after recording was completed to allow post hoc identification of the recording site (only recordings made from CA2 were kept for analysis).

Afferent stimulation consisted of constant current square wave pulses 30 - 500 µA in amplitude (set to 40% of maximal FP response) and 100 µsec in duration. Pre-conditioning baseline recordings of evoked FP peak amplitudes were made at a stimulation frequency of 0.1 Hz for 10 min. This was followed by a 20 minute period of synaptic conditioning, consisting of three stimulus trains of 100Hz for 1 sec, interleaved with two 10 min rest periods without stimulation (Dasgupta et al., 2017; “STET” protocol). Finally, post-conditioning evoked FP peak amplitudes were evaluated at 0.1 Hz for a period of 60 min.

All recordings were made with a MultiClamp 700B amplifier, digitized at 20 kHz with a Digidata 1440A and recorded using Clampex 10.7 software (Axon Instruments, Molecular Devices). Recordings of evoked FP peak amplitudes were measured as the difference between baseline and peak (analyzed with a 1 msec smoothing window). Any recordings with an unstable baseline (linear best fit of all preconditioning FP peak amplitudes had an $r^2 > 0.2$) were discarded. Only one recording was made from each slice, so that a single stimulation protocol was applied in each case.

Data was analyzed using Clampfit 10.7 software (Axon Instruments, Molecular Devices). We assessed plasticity of the FP response in each slice by calculating a post/pre ratio (the average FP peak amplitude for the last 5 minutes of post-conditioning divided by the average FP peak amplitude for the last 5 minutes of pre-

conditioning); which we defined as LTD for a significant ($p < 0.05$, *t*-test) decrease (>10%) in post/pre ratio, LTP for a significant increase (>10%) in post/pre ratio; or no change (not significantly different, or <10% change) in post/pre ratio. Data displayed as time plots show values for normalized FP peak amplitudes averaged over 1 minute intervals (i.e. each data point represents the average of 6 data points collected at 0.1 Hz).

Posthoc immunofluorescence staining was used to validate the recording site in area CA2 (Helton 2019 PMID: 30067288). After recording, slices were post-fixed in 4% paraformaldehyde for 12-48 hours then transferred to 1X PBS. Slices were permeabilized and blocked overnight with 3% Normal Goat Serum (NGS) in 1X PBS-0.3% Triton X-100 (0.3% PBST) before 2-3 day incubation with primary antibodies at 4C for PCP4 (1:250, Invitrogen Cat# PA5-52209, RRID:AB_2645298) or NECAB2 (1:250, Novus Cat# NBP1-84002, RRIS:AB_11028373). Slices were washed in 0.3% PBST several times and then incubated with AlexaFluor goat anti rabbit 633 (1:250, Sigma Cat# SAB4600141) overnight. After washes with 0.3% PBST, slices were stained with DAPI (Sigma Aldrich D9542, 1:10,000 in PBS) incubated for 30 min in 60% TDE prior to imaging cleared slices weighted with harps in a 6 well glass bottom plate (Cellvis P06-1.5H-N) on an Leica Thunder microscope at 20X.

Immunofluorescence

Mice were anesthetized with 150 mg/kg sodium pentobarbital and transcardially perfused with 15-20ml of ice-cold 4% paraformaldehyde. Brains were dissected and post-fixed for at least 24 hours before sectioning 40 µm thick sections in the horizontal plane on a vibratome (Leica VT1000S). All brain sections immunostained with MCU were washed in 1X PBS-0.1% Triton X-100 (0.1% PBST) before they underwent antigen retrieval by boiling free floating sections for 5 min in 1 ml of nanopure water, followed by a permeabilization step in 1X 0.1% PBST for 15 min at room temperature. All sections were then blocked for 1 hour in 5% Normal Goat Serum (NGS) in 0.1% PBST. Sections were incubated overnight at 4C (18-24 hours) with primary antibodies: rabbit-anti-MCU (1:2000, Novus Cat# NBP2-76948, Lot# H660681004, RRID:AB_2924913) and mouse-anti-RGS14 (1:500, NeuroMab Cat# 75–170, RRID:AB_2877352). Sections were then washed in 0.1% PBST several times and blocked for 30 minutes in 5% NGS in 0.1% PBST. Sections were incubated for 2 hours at room temperature in secondary antibodies (1:500, Invitrogen, AlexaFluors goat anti rabbit 546 Cat# A11035 and goat anti mouse 488 Cat# A11029) followed by several washes in 0.1% PBST and a final wash in 1X PBS.

cKO Validation

Fig. 1 includes MCU histology data from XX mice aged 8-16 weeks and 2 mice aged 32-62 weeks per genotype. The results from older mice did not significantly differ from younger mice. 20X (0.8 NA) 16 bit images of MCU and RGS14 immunolabeling were acquired on a Leica Thunder epifluorescence microscope (Leica DMi 8) using identical acquisition parameters for CTL and cKO and Lightning computationally clearing. MCU fluorescence was quantified in FIJI (v. 2.1.0/1.53c, NIH) (Shindelin et al., 2012) using max projected images from 3-5 sections per animal. CA2 neurons were identified via RGS14 labeling. A line ROI was drawn along the length of CA2 neurons (line length 650 µm, drawn at the end of the mossy fiber track with the start of the line being in SO and the midpoint of the line at the middle of SR), CA1 neurons (line length 700 µm, starting at SO with the midpoint of the line at the middle of SR), and DG granule neurons (line length 300 µm, starting at the granule cell body layer, with up to 75 µm covering the cell body layer when possible and the rest of the line on the molecular layer). Fluorescence values along the line were obtained using the FIJI Analyze and Plot Profile functions. For the neighboring cortex, a 400 µm x 400 µm ROI was cropped out of the original image and fluorescence intensity was measured using the Measure function in Fiji. Fluorescence background noise was subtracted for all regions using the negative control (no primary antibody) sections. Due to differences in the length of the CA regions along the dorsal-ventral axis, some of the ROI lines yielded zero values from the line being beyond the image border. These values were removed before averaging across sections per animal. The data were then binned by 10 microns length and averaged across sections to obtain one average fluorescence by distance line plot per animal. The data were then normalized to the CTL animals

run in the same IHC cohort. In order to compare across subregions, the peak binned value representing the cell body layer per section was averaged across sections per animal, and compared across regions such that every animal is represented in each region. MCU cKO was further validated through quantification of CA2 cell count using the Cell Counter tool in Fiji. An equal z-stack size was used for all images and cell bodies that expressed MCU and/or RGS14 were manually counted in each of these z sections. Experimenters were blind to genotype through the analyses and used RGS14 to guide placement of lines and cell counts. However, due to the obvious deletion of MCU expression in CA2 neurons, experimental bias could not be completely eliminated.

Protein-retention Expansion Microscopy (ProExM)

40 µm horizontal mouse brain sections were immunostained then expanded with 4X protein expansion microscopy (ProExM) as previously described in Campbell et al. 2021 using an *Amigo2*-EGFP line to selectively label CA2. Briefly, sections were treated as described above with the following modification. All sections were washed in PBS and blocked for at least 1 h in 5% Normal Goat Serum (NGS)/0.3% Triton-100x. Antibodies (MCU, 1:500 and Chicken anti-GFP, 1:500 Abcam ab13970) were diluted in blocking solution and sections were incubated for 72+ hours at room temperature (RT). After several rinses in PBS-T (0.3% Triton-100x), sections were incubated in secondary antibodies (1:500, Invitrogen AlexaFluors, goat anti chicken 488 Cat# A11039 and goat anti rabbit 546 Cat#A11035) for 48h at RT. Prior to imaging, adjacent unexpanded sections that were run simultaneously with expanded sections were washed in PBS-T and mounted under Vectashield fluorescence media to calculate pre-expansion nuclei diameters.

Sections to be expanded were incubated overnight in Acryloyl-X stock/PBS (1:100, ThermoFisher, A20770) at room temperature in the dark. All solutions were prepared as described by Asano et al. 2018. Following incubation, the slices were washed twice with PBS for 15 minutes each at room temperature. The gelation solution was prepared by adding 384 uL of monomer solution, 8 uL 4-Hydroxy-TEMPO inhibitor (1:200 w/v, Sigma Aldrich, 176141), 8uL TEMED accelerator (10% v/v, Sigma Aldrich, T7024), and lastly 8uL of APS initiator (10% w/v, Sigma Aldrich, 248614) for each section. Sections were incubated in the gelation solution for 30 minutes at 4C in the dark. Gelated sections were placed on gelation chambers constructed from microscope slides with coverslips as spacers. Our gelation chambers produce gels with the thickness of a single No. 1.5 coverslip (~0.15mm thick). The chambers were filled with gelation solution and allowed to incubate at 37C for 2 hours in a humidified container. Following gelation, the gelation chamber was deconstructed and the gel was carefully removed from the chamber using a coverslip and Proteinase K-free digestion solution. Gels were then placed in digestion solution containing proteinase K (8U/mL, New England BioLabs, P8107S) and digested for 4 hours at room temperature.

Gels were stained with DAPI (Sigma Aldrich, D9542; 1:10,000 in PBS) for 30 minutes at room temperature with shaking. Finally, the gels were washed twice with PBS for at least 20 minutes and either stored in PBS at 4C or fully expanded in npH20 for imaging. Images of CA2 SLM dendrites were acquired using 4X Super Resolution by Optical Pixel Reassignment (SoRa) on an inverted spinning disk confocal microscope (Yokogawa CSU-W1 SoRa/Nikon Ti2-E Microscope) equipped with Hamamatsu Fusion BT cameras, and 20X water (0.95 NA. WD 1.0 mm) or 60X oil (1.49 NA. WD 0.14 mm) immersion lenses.

Scanning Electron Microscopy

This protocol was adapted from the protocol version 2 published by NCMIR at UCSD (Deerinck et al. 2022). Mice were anesthetized with sodium pentobarbital (euthanasia solution, 150mg/kg) and perfused with ice-cold 0.1M cacodylate buffer pH 7.4 containing 2.5% glutaraldehyde, 2% paraformaldehyde with 2mM calcium chloride for 3 minutes. The brain was removed and fixed overnight at 4C in the same fixative before vibratome sectioning (Leica VT1000S) into 350-micron thick sections in the 0.1M cacodylate buffer pH 7.4 with 2mM calcium chloride. Sections were placed back in fixative for microdissection three days later. Hemisected brain sections were placed on wax paper with a drop of fixative and a 2mm x 2mm hippocampal microdissection was obtained per brain and placed back in fixative for further processing. Tissues were postfixed with 1.5 % potassium ferrocyanide plus 2% osmium tetroxide then en bloc stained with incubations in thiocarbohydrazide

solution, osmium tetroxide, uranyl acetate, and Walton's lead aspartate. Dehydration was performed by an ethanol gradient and finished in propylene oxide. Tissues were embedded in Epon 812. The embedded tissues were sectioned to 120 nm (Leica EM UC7 ultramicrotome), mounted on a silicon wafer, and imaged in a ThermoFisher Aprea Volumescope at 2nm pixel size. Three 150 x 150 μm regions of interest were obtained per section (basal, proximal, distal CA2 dendrites) from MCU cKO and CTL mice. A representative EM hippocampal section with ROIs drawn is shown in Figure 3A.

Analysis of SEM images with Biodock

Regions of interest (ROIs, 150 x 150 μm) in SO, SR and SLM of CA2 in three 120 nm sections from each of three CTL and cKO mice were analyzed. The larger ROIs were acquired as 14 x 20 100 μm^2 tiles with 10% overlap for stitching (~12.2 x 8.2 μm). Every 8th tile was selected for analysis to avoid analyzing overlapping tiles. A similar sampling scheme was used for a handful of images that were acquired as 2 x 2 6,700 μm^2 tiles with 10% overlap, resulting in the same-sized 100 μm^2 tiles for analysis. Image sampling and processing were done in batches with a custom Python code. Images were inverted if necessary, and a Gaussian blur with a radius of 2 nm was applied to all EM images for training and analysis. Tiles were excluded from analysis if they had poor image quality, significant artifacts or rips, contained only axonal tracts or cell bodies, or were otherwise unfit to analyze. A total of 1,559 tiles (~156,000 μm^2) were analyzed across the 6 mice.

To train the Biodock AI, we separated a subset of data (~1% of the total dataset) for training, making sure to include training data from each layer and genotype in the analysis, as well as undesired elements such as cell bodies, artifacts and blank spaces. We selected an appropriate tile size in Biodock (4000 x 4000 pixels) and labeled all dendritic mitochondria in the training images as an object type class. To be counted as a dendritic mitochondria, the object must have distinct borders, a solid dark fill, and be located inside a clear dendrite segment not bordered by myelin or containing synaptic vesicles. We excluded fragments of mitochondria at image edges or if the identity or location of the object was ambiguous. We proceeded to train the AI on the dendritic mitochondria object class, allowing augmentations such as image flipping and brightness/contrast adjustments. We assessed the AI's performance with a manual spot check on a test dataset of about 2% of the final dataset. The average number of mistakes per tile was counted by category. Categories included missing dendritic mitochondria, border errors, object merging, detection of axonal or soma mitochondria, and identification of non-mitochondrial elements like myelin. The overall sensitivity of the AI model in correcting identifying dendritic mitochondria was 92.2%.

The trained AI was then used to analyze the final dataset of 3 CTL and 3 cKO mice. We configured the AI project settings to define the analysis metrics of interest and set a confidence threshold of 0.4. A size threshold was applied to exclude mitochondrial objects smaller than 0.01 μm or larger than 2.1 μm, which reflects the minimum and maximum area of visually confirmed mitochondria objects in the dataset. All pixel measurements were converted to microns for length and area, and the aspect ratio was calculated by dividing the short axis by the long axis of each object. Total mitochondrial count and total mitochondrial area were summed per 100 μm^2 tile, and a nearest neighbor analysis was performed with the KDTree function in the Python package Scipy (Virtanen et al., 2020) to determine mitochondrial euclidean distances. Data for the plots in Figure 3 were normalized to the combined mean of the control. Standard two-way ANOVAs and non-parametric posthoc tests with Sidak's correction were run with the Pingouin package (Vallat, 2018) on the individual mitochondria for our metrics of interest.

Golgi staining

Mice aged 8-16 weeks were perfused and postfixed for at least 24 hours with 2.5% glutaraldehyde/2% paraformaldehyde. Then, brains were dissected in 5 mm^3 blocks and stained with FD Rapid GolgiStain™ Kit (CAT# PK401) as described in the product manual. A subset of the mice used for Golgi analysis were also

used for SEM and processed as 350 µm thick slices as described above. Thick brain slices were wrapped with uniformly thicker 2 mm brain sections and processed as tissue bundles as described in Harris et al. (PMID: 6997641) for Golgi-Cox impregnation using the same kit. Both 5 mm^3 blocks and 350 µm slices were cryoprotected in 30% sucrose for 4-5 days until they sank. Then they were blocked in OCT and cryosectioned at 40 µm thick in the horizontal plane using Leica Cryostat (Leica CM1860). CTL (n=8) and cKO (n=8) brains were processed in pairs containing each genotype to avoid any potential batch issues. High resolution 63X (NA 1.4) images of CA2 SLM (up to 25µm total on Z-axis, optical section thickness= 0.21µm) were acquired using brightfield microscopy on a Leica Thunder microscope. Individual dendrites in the plane were cropped from the 63X images using Fiji and randomly chosen for analysis. Fiji plugin “Dendritic spine counter” was used to measure dendrite length, total spine count and spine density (number of spines / length of the dendrite) from the cropped dendrites. In summary, ~200 dendrites were analyzed for spine density in total for both groups. A subset of dendritic segments (~30-40 µm in length) from both CTL and cKO mice was quantified for spine morphology using the same plugin in Fiji. Individual spines were manually classified based on visual characteristics and features as filopodia, thin, stubby, mushroom and branched (two heads) on 2D average projection images and validated with the Z-stacks to confirm the geometry of spine shapes (Risher et al., 2014) Protrusions from the dendrites that were long and thin were marked as filopodia, and protrusions with a small round tip at the end were classified as thin spines. Thick protrusions with larger, rounded head and relatively narrower neck were marked as mushrooms, and small protrusions without any visible neck were classified as stubby. As the staining is dark and opaque in this technique, spines right above and beneath the dendrites were not visualized and no attempt was made to account for these spines. In total, ~800 spines were classified per genotype. For plots (Fig 3E & F), thin and filopodia spines were combined as immature spines and stubby, mushroom, and branched spines were combined as mature spine class.

Statistical analyses

A custom Python code was written to parse the segmented data from Biodock and get the aspect ratio, count, total area and distance to nearest neighbor for the dendritic mitochondria objects. Statistical analyses were done in python (v3.11) or Prism (Graphpad Prism 10) with an alpha of 0.05 considered significant.
Data are presented as animal averages, unless otherwise indicated in the legend.

DECLARATIONS

Funding

Research reported in this publication was supported by the National Institute of Mental Health of the NIH under award R01MH124997 to S.F. and by startup funds provided by Virginia Tech. The Serial Block Face Scanning Electron Microscope was acquired under NIH award 1S10OD026838-01A1. The funders had no role in the design of the study and collection, analysis, and interpretation of data and in writing the manuscript.

Authors' contributions

Conceptualization, SF; Methodology, CE, KEP, DVG, MLC, MMA, NA, LAC, RT, SF, QSF; Formal Analysis, CE, KEP, DVG, MLC, MMA, NA, LAC, RT, SF, QSF; Investigation, CE, KEP, DVG, MLC, MMA, NA, LAC, RT, SF, QSF; Writing – Original Draft, KEP, SF; Writing – Review & Editing, KEP, DVG, MLC, MMA, NA, RT, SF, QSF; Visualization, KEP, MLC, MMA, RT, SF, QSF; Supervision, SF; Funding Acquisition, SF.

Data availability

Data is available from the authors upon request.

Acknowledgements

We thank the Virginia Tech animal care staff for their support. The authors also acknowledge resources and support from the Cellular and Molecular Imaging Core, part of the Fralin Biomedical Research Institute at VTC. This research would not be possible without the use of the Thermo Fisher Aprea 2 Serial Blockface Scanning

Electron Microscope (NIH award 1S10OD026838-01A1) and Christie Lacy for acquiring the micrographs used for the data shown in Figure 4 Supplemental Figure 2.

Conflict of interest

The authors declare that they have no competing interests.

REFERENCES

1. Alexander, Georgia M, Logan Y Brown, Shannon Farris, Daniel Lustberg, Caroline Pantazis, Bernd Gloss, Nicholas W Plummer, Patricia Jensen, and Serena M Dudek. “CA2 Neuronal Activity Controls Hippocampal Low Gamma and Ripple Oscillations.” *eLife* 7 (November 2, 2018): e38052. https://doi.org/10.7554/eLife.38052.

2. Asano, Shoh M., Ruixuan Gao, Asmamaw T. Wassie, Paul W. Tillberg, Fei Chen, and Edward S. Boyden. “Expansion Microscopy: Protocols for Imaging Proteins and RNA in Cells and Tissues.” *Current Protocols in Cell Biology* 80, no. 1 (September 2018). https://doi.org/10.1002/cpcb.56.

3. Ashrafi, Ghazaleh, Jaime de Juan-Sanz, Ryan J. Farrell, and Timothy A. Ryan. “Molecular Tuning of the Axonal Mitochondrial Ca2+ Uniporter Ensures Metabolic Flexibility of Neurotransmission.” *Neuron* 105, no. 4 (February 2020): 678-687.e5. https://doi.org/10.1016/j.neuron.2019.11.020.

4. Bas-Orth, Carlos, Justus Schneider, Andrea Lewen, Jamie McQueen, Kerstin Hasenpusch-Theil, Thomas Theil, Giles E Hardingham, Hilmar Bading, and Oliver Kann. “The Mitochondrial Calcium Uniporter Is Crucial for the Generation of Fast Cortical Network Rhythms.” *Journal of Cerebral Blood Flow & Metabolism* 40, no. 11 (November 2020): 2225–39. https://doi.org/10.1177/0271678X19887777.

5. Baughman, Joshua M., Fabiana Perocchi, Hany S. Girgis, Molly Plovanich, Casey A. Belcher-Timme, Yasemin Sancak, X. Robert Bao, et al. “Integrative Genomics Identifies MCU as an Essential Component of the Mitochondrial Calcium Uniporter.” *Nature* 476, no. 7360 (August 2011): 341–45. https://doi.org/10.1038/nature10234.

6. Berry, Kalen P., and Elly Nedivi. “Spine Dynamics: Are They All the Same?” *Neuron* 96, no. 1 (September 27, 2017): 43–55. https://doi.org/10.1016/j.neuron.2017.08.008.

7. Biodock, AI Software Platform. Biodock 2023. Available from www.biodock.ai.

8. Campbell, Logan A., Katy E. Pannoni, Niesha A. Savory, Dinesh Lal, and Shannon Farris. “Protein-Retention Expansion Microscopy for Visualizing Subcellular Organelles in Fixed Brain Tissue.” *Journal of Neuroscience Methods* 361 (September 2021): 109285. https://doi.org/10.1016/j.jneumeth.2021.109285.

9. Chaudhuri, D., Y. Sancak, V.K. Mootha, and D.E. Clapham. “MCU Encodes the Pore Conducting Mitochondrial Calcium Currents.” *eLife* 2013, no. 2 (2013). https://doi.org/10.7554/eLife.00704.

10. Chevaleyre, Vivien, and Steven A. Siegelbaum. “Strong CA2 Pyramidal Neuron Synapses Define a Powerful Disynaptic Cortico-Hippocampal Loop.” *Neuron* 66, no. 4 (May 2010): 560–72. https://doi.org/10.1016/j.neuron.2010.04.013.

11. Contreras, Laura, and Jorgina Satrústegui. “Calcium Signaling in Brain Mitochondria: Interplay of Malate Aspartate NADH Shuttle and Calcium Uniporter/Mitochondrial Dehydrogenase Pathways.” *The*

Journal of Biological Chemistry 284, no. 11 (March 13, 2009): 7091–99. https://doi.org/10.1074/jbc.M808066200.

12. Dasgupta, Ananya, Nimmi Baby, Kumar Krishna, Muhammad Hakim, Yuk Peng Wong, Thomas Behnisch, Tuck Wah Soong, and Sreedharan Sajikumar. “Substance P Induces Plasticity and Synaptic Tagging/Capture in Rat Hippocampal Area CA2.” *Proceedings of the National Academy of Sciences of the United States of America* 114, no. 41 (October 1, 2017): E8741–49. https://doi.org/10.1073/pnas.1711267114.

13. Dasgupta, Ananya, Yu Jia Lim, Krishna Kumar, Nimmi Baby, Ka Lam Karen Pang, Amrita Benoy, Thomas Behnisch, and Sreedharan Sajikumar. “Group III Metabotropic Glutamate Receptors Gate Long-Term Potentiation and Synaptic Tagging/Capture in Rat Hippocampal Area CA2.” *eLife* 9 (April 20, 2020): e55344. https://doi.org/10.7554/eLife.55344.

14. Delgado, Thomas, Ronald S. Petralia, David W. Freeman, Miloslav Sedlacek, Ya-Xian Wang, Stephan D. Brenowitz, Shu-Hsien Sheu, et al. “Comparing 3D Ultrastructure of Presynaptic and Postsynaptic Mitochondria.” *Biology Open* 8, no. 8 (August 15, 2019): bio044834. https://doi.org/10.1242/bio.044834.

15. “Dendritic Spine Counter Plugin for ImageJ.” Accessed November 7, 2023. https://www.abstractsonline.com/pp8/#!/10485/presentation/19804.

16. Devine, Michael J., and Josef T. Kittler. “Mitochondria at the Neuronal Presynapse in Health and Disease.” *Nature Reviews Neuroscience* 19, no. 2 (February 2018): 63–80. https://doi.org/10.1038/nrn.2017.170.

17. Devine, Michael J., Blanka R. Szulc, Jack H. Howden, Guillermo López-Doménech, Arnaud Ruiz, and Josef T. Kittler. “Mitochondrial Ca2+ Uniporter Haploinsufficiency Enhances Long-Term Potentiation at Hippocampal Mossy Fibre Synapses.” *Journal of Cell Science* 135, no. 22 (November 15, 2022): jcs259823. https://doi.org/10.1242/jcs.259823.

18. Divakaruni, Sai Sachin, Adam M. Van Dyke, Ramesh Chandra, Tara A. LeGates, Minerva Contreras, Poorna A. Dharmasri, Henry N. Higgs, Mary Kay Lobo, Scott M. Thompson, and Thomas A. Blanpied. “Long-Term Potentiation Requires a Rapid Burst of Dendritic Mitochondrial Fission during Induction.” *Neuron* 100, no. 4 (November 2018): 860-875.e7. https://doi.org/10.1016/j.neuron.2018.09.025.

19. Dudek, Serena M., Georgia M. Alexander, and Shannon Farris. “Rediscovering Area CA2: Unique Properties and Functions.” *Nature Reviews. Neuroscience* 17, no. 2 (February 2016): 89–102. https://doi.org/10.1038/nrn.2015.22.

20. Engert, Florian, and Tobias Bonhoeffer. “Dendritic Spine Changes Associated with Hippocampal Long-Term Synaptic Plasticity.” *Nature* 399, no. 6731 (May 1999): 66–70. https://doi.org/10.1038/19978.

21. Evans, Paul R., Paula Parra-Bueno, Michael S. Smirnov, Daniel J. Lustberg, Serena M. Dudek, John R. Hepler, and Ryohei Yasuda. “RGS14 Restricts Plasticity in Hippocampal CA2 by Limiting Postsynaptic Calcium Signaling.” *eNeuro*, May 21, 2018. https://doi.org/10.1523/ENEURO.0353-17.2018.

22. Faitg, Julie, Clay Lacefield, Tracey Davey, Kathryn White, Ross Laws, Stylianos Kosmidis, Amy K. Reeve, Eric R. Kandel, Amy E. Vincent, and Martin Picard. “3D Neuronal Mitochondrial Morphology in Axons, Dendrites, and Somata of the Aging Mouse Hippocampus.” *Cell Reports* 36, no. 6 (August 2021): 109509. https://doi.org/10.1016/j.celrep.2021.109509.

23. Farris, Shannon, James M. Ward, Kelly E. Carstens, Mahsa Samadi, Yu Wang, and Serena M. Dudek. “Hippocampal Subregions Express Distinct Dendritic Transcriptomes That Reveal Differences in Mitochondrial Function in CA2.” *Cell Reports* 29, no. 2 (October 2019): 522-539.e6. https://doi.org/10.1016/j.celrep.2019.08.093.

24. Giorgi, Carlotta, Diego De Stefani, Angela Bononi, Rosario Rizzuto, and Paolo Pinton. “Structural and Functional Link between the Mitochondrial Network and the Endoplasmic Reticulum.” *The International Journal of Biochemistry & Cell Biology* 41, no. 10 (October 2009): 1817–27. https://doi.org/10.1016/j.biocel.2009.04.010.

25. Glaser, Edmund M., and Hendrik Van der Loos. “Analysis of Thick Brain Sections by Obverse—Reverse Computer Microscopy: Application of a New, High Clarity Golgi—Nissl Stain.” *Journal of Neuroscience Methods* 4, no. 2 (August 1, 1981): 117–25. https://doi.org/10.1016/0165-0270(81)90045-5.

26. Granatiero, Veronica, Marco Pacifici, Anna Raffaello, Diego De Stefani, and Rosario Rizzuto. “Overexpression of Mitochondrial Calcium Uniporter Causes Neuronal Death.” *Oxidative Medicine and Cellular Longevity* 2019 (2019): 1681254. https://doi.org/10.1155/2019/1681254.

27. Groten, Christopher J., and Brian A. MacVicar. “Mitochondrial Ca2+ Uptake by the MCU Facilitates Pyramidal Neuron Excitability and Metabolism during Action Potential Firing.” *Communications Biology* 5, no. 1 (September 2, 2022): 900. https://doi.org/10.1038/s42003-022-03848-1.

28. Hamilton, James, Tatiana Brustovetsky, Jacob E. Rysted, Zhihong Lin, Yuriy M. Usachev, and Nickolay Brustovetsky. “Deletion of Mitochondrial Calcium Uniporter Incompletely Inhibits Calcium Uptake and Induction of the Permeability Transition Pore in Brain Mitochondria.” *Journal of Biological Chemistry* 293, no. 40 (October 5, 2018): 15652–63. https://doi.org/10.1074/jbc.RA118.002926.

29. Harris, Julia J., Renaud Jolivet, and David Attwell. “Synaptic Energy Use and Supply.” *Neuron* 75, no. 5 (September 6, 2012): 762–77. https://doi.org/10.1016/j.neuron.2012.08.019.

30. Harris, K. M., W. L. Cruce, W. T. Greenough, and T. J. Teyler. “A Golgi Impregnation Technique for Thin Brain Slices Maintained in Vitro.” *Journal of Neuroscience Methods* 2, no. 4 (August 1980): 363–71. https://doi.org/10.1016/0165-0270(80)90003-5.

31. Helton, Thomas D., Meilan Zhao, Shannon Farris, and Serena M. Dudek. “Diversity of Dendritic Morphology and Entorhinal Cortex Synaptic Effectiveness in Mouse CA2 Pyramidal Neurons.” *Hippocampus* 29, no. 2 (February 2019): 78–92. https://doi.org/10.1002/hipo.23012.

32. Hill, Travis C., and Karen Zito. “LTP-Induced Long-Term Stabilization of Individual Nascent Dendritic Spines.” *Journal of Neuroscience* 33, no. 2 (January 9, 2013): 678–86. https://doi.org/10.1523/JNEUROSCI.1404-12.2013.

33. Hitti, Frederick L., and Steven A. Siegelbaum. “The Hippocampal CA2 Region Is Essential for Social Memory.” *Nature* 508, no. 7494 (April 2014): 88–92. https://doi.org/10.1038/nature13028.

34. Holtmaat, Anthony, and Karel Svoboda. “Experience-Dependent Structural Synaptic Plasticity in the Mammalian Brain.” *Nature Reviews Neuroscience* 10, no. 9 (September 2009): 647–58. https://doi.org/10.1038/nrn2699.

35. Huntington, Taylor E., and Rahul Srinivasan. “Astrocytic Mitochondria in Adult Mouse Brain Slices Show Spontaneous Calcium Influx Events with Unique Properties.” *Cell Calcium* 96 (June 2021): 102383. https://doi.org/10.1016/j.ceca.2021.102383.

36. Kamer, Kimberli J., and Vamsi K. Mootha. “The Molecular Era of the Mitochondrial Calcium Uniporter.” *Nature Reviews Molecular Cell Biology* 16, no. 9 (September 2015): 545–53. https://doi.org/10.1038/nrm4039.

37. Kasai, Haruo, Masanori Matsuzaki, Jun Noguchi, Nobuaki Yasumatsu, and Hiroyuki Nakahara. “Structure–Stability–Function Relationships of Dendritic Spines.” *Trends in Neurosciences* 26, no. 7 (July 1, 2003): 360–68. https://doi.org/10.1016/S0166-2236(03)00162-0.

38. Kwong, Jennifer Q., Xiyuan Lu, Robert N. Correll, Jennifer A. Schwanekamp, Ronald J. Vagnozzi, Michelle A. Sargent, Allen J. York, Jianyi Zhang, Donald M. Bers, and Jeffery D. Molkentin. “The Mitochondrial Calcium Uniporter Selectively Matches Metabolic Output to Acute Contractile Stress in the Heart.” *Cell Reports* 12, no. 1 (July 2015): 15–22. https://doi.org/10.1016/j.celrep.2015.06.002.

39. Lewis, Tommy L., Seok-Kyu Kwon, Annie Lee, Reuben Shaw, and Franck Polleux. “MFF-Dependent Mitochondrial Fission Regulates Presynaptic Release and Axon Branching by Limiting Axonal Mitochondria Size.” *Nature Communications* 9, no. 1 (December 2018): 5008. https://doi.org/10.1038/s41467-018-07416-2.

40. Li, Zheng, Ken-Ichi Okamoto, Yasunori Hayashi, and Morgan Sheng. “The Importance of Dendritic Mitochondria in the Morphogenesis and Plasticity of Spines and Synapses.” *Cell* 119, no. 6 (December 2004): 873–87. https://doi.org/10.1016/j.cell.2004.11.003.

41. Liang, Nan, Peng Wang, Shilei Wang, Shuhong Li, Yu Li, Jinying Wang, and Min Wang. “Role of Mitochondrial Calcium Uniporter in Regulating Mitochondrial Fission in the Cerebral Cortexes of Living Rats.” *Journal of Neural Transmission* 121, no. 6 (June 1, 2014): 593–600. https://doi.org/10.1007/s00702-014-1166-6.

42. Llorente-Folch, I., C. B. Rueda, B. Pardo, G. Szabadkai, M. R. Duchen, and J. Satrustegui. “The Regulation of Neuronal Mitochondrial Metabolism by Calcium: Regulation of Neuronal Mitochondrial Metabolism.” *The Journal of Physiology* 593, no. 16 (August 15, 2015): 3447–62. https://doi.org/10.1113/JP270254.

43. Lopez-Rojas, Jeffrey, Christopher A. de Solis, Felix Leroy, Eric R. Kandel, and Steven A. Siegelbaum. “A Direct Lateral Entorhinal Cortex to Hippocampal CA2 Circuit Conveys Social Information Required for Social Memory.” *Neuron* 110, no. 9 (May 2022): 1559-1572.e4. https://doi.org/10.1016/j.neuron.2022.01.028.

44. Matsuzaki, Masanori, Naoki Honkura, Graham C. R. Ellis-Davies, and Haruo Kasai. “Structural Basis of Long-Term Potentiation in Single Dendritic Spines.” *Nature* 429, no. 6993 (June 2004): 761–66. https://doi.org/10.1038/nature02617.

45. Nicoll, Roger A. “A Brief History of Long-Term Potentiation.” *Neuron* 93, no. 2 (January 18, 2017): 281–90. https://doi.org/10.1016/j.neuron.2016.12.015.

46. Pan, Xin, Jie Liu, Tiffany Nguyen, Chengyu Liu, Junhui Sun, Yanjie Teng, Maria M Fergusson, et al. “The Physiological Role of Mitochondrial Calcium Revealed by Mice Lacking the Mitochondrial Calcium

Uniporter (MCU)." *Nature Cell Biology* 15, no. 12 (December 2013): 1464–72. https://doi.org/10.1038/ncb2868.

47. Pannoni, Katy E., Daniela Gil, Mikel L. Cawley, Mayd M. Alsalman, Logan A. Campbell, and Shannon Farris. "Layer-specific Mitochondrial Diversity across Hippocampal CA2 Dendrites." *Hippocampus* 33, no. 3 (March 2023): 182–96. https://doi.org/10.1002/hipo.23512.

48. Popov, Victor, Nikolai I. Medvedev, Heather A. Davies, and Michael G. Stewart. "Mitochondria Form a Filamentous Reticular Network in Hippocampal Dendrites but Are Present as Discrete Bodies in Axons: A Three-Dimensional Ultrastructural Study." *The Journal of Comparative Neurology* 492, no. 1 (November 7, 2005): 50–65. https://doi.org/10.1002/cne.20682.

49. Qiu, Jing, Yan-Wei Tan, Anna M. Hagenston, Marc-Andre Martel, Niclas Kneisel, Paul A. Skehel, David J. A. Wyllie, Hilmar Bading, and Giles E. Hardingham. "Mitochondrial Calcium Uniporter Mcu Controls Excitotoxicity and Is Transcriptionally Repressed by Neuroprotective Nuclear Calcium Signals." *Nature Communications* 4, no. 1 (October 2013): 2034. https://doi.org/10.1038/ncomms3034.

50. Rangaraju, Vidhya, Marcel Lauterbach, and Erin M. Schuman. "Spatially Stable Mitochondrial Compartments Fuel Local Translation during Plasticity." *Cell* 176, no. 1–2 (January 10, 2019): 73-84.e15. https://doi.org/10.1016/j.cell.2018.12.013.

51. Risher, W. Christopher, Tuna Ustunkaya, Jonnathan Singh Alvarado, and Cagla Eroglu. "Rapid Golgi Analysis Method for Efficient and Unbiased Classification of Dendritic Spines." *PLoS ONE* 9, no. 9 (September 10, 2014): e107591. https://doi.org/10.1371/journal.pone.0107591.

52. Rizzuto, R., P. Pinton, W. Carrington, F. S. Fay, K. E. Fogarty, L. M. Lifshitz, R. A. Tuft, and T. Pozzan. "Close Contacts with the Endoplasmic Reticulum as Determinants of Mitochondrial Ca2+ Responses." *Science (New York, N.Y.)* 280, no. 5370 (June 12, 1998): 1763–66. https://doi.org/10.1126/science.280.5370.1763.

53. Rizzuto, Rosario, Diego De Stefani, Anna Raffaello, and Cristina Mammucari. "Mitochondria as Sensors and Regulators of Calcium Signalling." *Nature Reviews Molecular Cell Biology* 13, no. 9 (September 2012): 566–78. https://doi.org/10.1038/nrm3412.

54. Satrústegui, Jorgina, and Lasse K. Bak. "Fluctuations in Cytosolic Calcium Regulate the Neuronal Malate–Aspartate NADH Shuttle: Implications for Neuronal Energy Metabolism." *Neurochemical Research* 40, no. 12 (December 1, 2015): 2425–30. https://doi.org/10.1007/s11064-015-1652-8.

55. Schindelin, Johannes, Ignacio Arganda-Carreras, Erwin Frise, Verena Kaynig, Mark Longair, Tobias Pietzsch, Stephan Preibisch, et al. "Fiji: An Open-Source Platform for Biological-Image Analysis." *Nature Methods* 9, no. 7 (July 2012): 676–82. https://doi.org/10.1038/nmeth.2019.

56. Smith, Heather L, Jennifer N Bourne, Guan Cao, Michael A Chirillo, Linnaea E Ostroff, Deborah J Watson, and Kristen M Harris. "Mitochondrial Support of Persistent Presynaptic Vesicle Mobilization with Age-Dependent Synaptic Growth after LTP." *eLife* 5 (December 19, 2016): e15275. https://doi.org/10.7554/eLife.15275.

57. Sprenger, Hans-Georg, and Thomas Langer. "The Good and the Bad of Mitochondrial Breakups." *Trends in Cell Biology* 29, no. 11 (November 2019): 888–900. https://doi.org/10.1016/j.tcb.2019.08.003.

58. Stoler, Ohad, Alexandra Stavsky, Yana Khrapunsky, Israel Melamed, Grace Stutzmann, Daniel Gitler, Israel Sekler, and Ilya Fleidervish. “Frequency- and Spike-Timing-Dependent Mitochondrial Ca2+ Signaling Regulates the Metabolic Rate and Synaptic Efficacy in Cortical Neurons.” Edited by Sacha B Nelson, John R Huguenard, Sacha B Nelson, and Bruce P Bean. *eLife* 11 (February 22, 2022): e74606. https://doi.org/10.7554/eLife.74606.

59. Stowers, R.Steven, Laura J. Megeath, Jolanta Górska-Andrzejak, Ian A. Meinertzhagen, and Thomas L. Schwarz. “Axonal Transport of Mitochondria to Synapses Depends on Milton, a Novel Drosophila Protein.” *Neuron* 36, no. 6 (December 2002): 1063–77. https://doi.org/10.1016/S0896-6273(02)01094-2.

60. Tang, Yun-gui, and Robert S. Zucker. “Mitochondrial Involvement in Post-Tetanic Potentiation of Synaptic Transmission.” *Neuron* 18, no. 3 (March 1, 1997): 483–91. https://doi.org/10.1016/S0896-6273(00)81248-9.

61. Vallat, Raphael. “Pingouin: Statistics in Python.” *Journal of Open Source Software* 3, no. 31 (November 19, 2018): 1026. https://doi.org/10.21105/joss.01026.

62. Virga, Daniel M., Stevie Hamilton, Bertha Osei, Abigail Morgan, Emiliano Zamponi, Natalie J. Park, Victoria L. Hewitt, et al. “Activity-Dependent Subcellular Compartmentalization of Dendritic Mitochondria Structure in CA1 Pyramidal Neurons.” bioRxiv, March 26, 2023. https://doi.org/10.1101/2023.03.25.534233.

63. Virtanen, Pauli, Ralf Gommers, Travis E. Oliphant, Matt Haberland, Tyler Reddy, David Cournapeau, Evgeni Burovski, et al. “SciPy 1.0: Fundamental Algorithms for Scientific Computing in Python.” *Nature Methods* 17, no. 3 (March 2020): 261–72. https://doi.org/10.1038/s41592-019-0686-2.

64. Voloshin, M, P. C. Romero, J. Parato. Dendritic Spine Counter plugin for ImageJ. Neuroscience 2021Annual Meeting. URL: https://www.abstractsonline.com/pp8/#!/10485/presentation/19804 (Accessed 11 April 2023).

65. Wescott, Andrew P., Joseph P. Y. Kao, W. Jonathan Lederer, and Liron Boyman. “Voltage-Energized Calcium-Sensitive ATP Production by Mitochondria.” *Nature Metabolism* 1, no. 10 (October 2019): 975–84. https://doi.org/10.1038/s42255-019-0126-8.

66. Zhao, Lantao, Shuhong Li, Shilei Wang, Ning Yu, and Jia Liu. “The Effect of Mitochondrial Calcium Uniporter on Mitochondrial Fission in Hippocampus Cells Ischemia/Reperfusion Injury.” *Biochemical and Biophysical Research Communications* 461, no. 3 (June 2015): 537–42. https://doi.org/10.1016/j.bbrc.2015.04.066.

67. Zhao, M., Y.-S. Choi, K. Obrietan, and S. M. Dudek. “Synaptic Plasticity (and the Lack Thereof) in Hippocampal CA2 Neurons.” *Journal of Neuroscience* 27, no. 44 (October 31, 2007): 12025–32. https://doi.org/10.1523/JNEUROSCI.4094-07.2007.